NUMERICAL SIMULATION OF SEISMIC WAVE PROPAGATION IN THE PRESENCE OF COMPLEX NEAR-SURFACE HETEROGENEITY INCLUDING SURFACE TOPOGRAPHY

A Thesis

by

JUNGRAK SON

Submitted to the Office of Graduate and Professional Studies of
Texas A&M University
in partial fulfillment of the requirements for the degree of

MASTER OF SCIENCE

Chair of Committee,	Richard L. Gibson, Jr.
Co-Chair of Committee,	Benchun Duan
Committee Member,	Yalchin Efendiev
Head of Department,	Rick J. Giardino

August 2015

Major Subject: Geophysics

ABSTRACT

Surface wave analysis and inversion have been developed to improve P-wave imaging for hydrocarbon reservoirs in land environments. This requires elastic wave modeling validation based on an accurate near-surface geology model. However, conventional modeling approaches with uniform grids pose significant challenges to represent complex geometry of near-surface heterogeneities and irregular surface topography. To solve this issue, numerical simulation of elastic wave propagation is implemented based on the spectral-element method, which is ideal for applying flexible unstructured grids. Locally-refined hybrid grids are used to describe the complex boundaries of subsurface structures, and refined grids are effective to reduce computational costs.

Three representative examples of geological features as near-surface heterogeneities are analyzed in seismic modeling with synthetic earth models. The structures are a shallow small scatterer, a collapsed karst structure and a low-velocity top layer with surface topography. The earth model geometry and material properties are based on the data from the recently released SEAM 2 project "arid model." The resulting seismograms show that scattered surface waves from the shallow velocity anomalies are affected by the shape of modeling grids, properties of filling materials, attenuation, and curved surface topography. Specifically, the shallow scatterer, which is filled with low-velocity materials, shows a significant amount of trapped seismic energy and generates multiple scattered surface waves. These unwanted waves from trapped energy are strongly based on the surface topography and attenuation factor, Q. Since scattered surface waves are sensitively affected by various geological features and modeling factors, advanced seismic forward modeling approaches should be used

for the accurate near-surface modeling. This study shows the capability and potential of the spectral-element method with advanced conforming grids to handle high impedance contrast boundaries for the analysis of interaction between the seismic wave scattering and complex heterogeneous shallow media. It will lead to improve distinguishing of seismic noise caused by shallow anomalies from the valuable signals associated with hydrocarbon reservoirs.

DEDICATION

To my beloved wife who has encouraged me to keep going forward.

TABLE OF CONTENTS

LIST OF FIGURES

LIST OF TABLES

1. INTRODUCTION

Land seismic activity is increasing around the world for onshore hydrocarbon reservoirs. However, the seismic data from land environments contain significant scattered surface waves, and they cause challenging problems in seismic interpretation. These unwanted waves are generated from complex near-surface heterogeneities. Dry riverbeds and subsurface collapsed karst structures are the representative examples of the near-surface heterogeneities (Keho and Kelamis, 2012), and they show the obvious seismic effects in the Arabian limestone deserts (Al-Husseini et al., 1981). A case study from Saudi Arabia (McNeely et al., 2012) showed how important the accurate near-surface model is to image low-relief structures, because the first 500 m of shallow geology in Saudi Arabia is very complex. Furthermore, the extreme low-velocity material properties in shallow layers is another challenging factor. Since their low-velocity material properties, strong seismic energy is trapped in shallow structures and generates unwanted multiple noises. This signal contamination masks the upcoming body wave reflections from deep structures, which should be interpreted. The seismic effects of shallow small scatterers have been studied in forward modeling (Almuhaidib and Toksoz, 2014), (Gelis et al., 2005), (Zeng et al., 2012) with simple synthetic near-surface models, and these studies show advanced approaches to analyze surface wave scattering. However, the near-surface of an arid region field environment is quite complex, so additional factors, such as complex geometry subsurface structures, or low-velocity sand layers on the free-surface with irregular topography, should be considered for accurate seismic forward modeling.

The most challenging parts in near-surface forward modeling are the complex geometry of subsurface structures and high impedance contrast. Even though most

seismic full waveform modeling relies on conventional finite-difference solutions, there are two critical limitations to apply them for near-surface modeling. Since finite-difference relies on regular Cartesian grids, the grids cannot conform to the complex geometry of near-surface heterogeneities, and the results are not accurate enough. Specifically, the irregular surface topography causes significant differences in surface wave propagation (Appelo and Petersson, 2009; Bohlen and Saenger, 2006; Robertsson, 1996; Tessmer et al., 1992), but finite-difference solutions with regular Cartesian grids suffer from the curved free-surface condition (Graves, 1996; Muir et al., 1992). Furthermore, the grid spacing on the entire model should be uniform, and it requires extremely fine grids and significant computational resources because of the near-surface low-velocity materials. Near-surface surface rocks in Saudi Arabia show about $1000 m/s$ velocity material property, and sands have much less properties $(500 \sim 1000 m/s)$ (Bridle et al., 2007). For example, a sand dune finite-difference modeling study (Yilmaz, 2013) used extreme fine grid spacing $(0.25m)$. However, it is not possible to use this excessive grid on an entire large-scale model with hydrocarbon reservoirs. Many other approaches have been developed to reduce computational costs in extreme fine grid modeling (Chung et al., 2011; Gibson et al., 2014; Ma et al., 2004; Reshetova et al., 2011) and they showed potential possibilities.

In this study, I applied locally-refined hybrid grids in complex near-surface synthetic earth models to analyze the seismic effects of shallow heterogeneities. To prevent dispersion error from unstructured grids, the spectral-element method for the elastic wave simulations has been used with 4th order basis functions. Resulting seismograms of three representative examples of geological features as near-surface heterogeneities (Figure 1.1): low-velocity top layer, shallow scatterers, collapsed karst structures, are compared to analyze the each seismic effect. Scattered surface waves from these anomalies are strongly dependent on modeling grid design, filling ma-

terials, attenuation factor, and topography. Specially, the shallow scatterer, which is filled with low-velocity materials, shows a significant amount of trapped seismic energy in the scatterer and generates multiple scattered surface waves. Amplitude of these unwanted waves from the scatterer, which acts as a secondary source, strongly relies on the variation of surface topography and attenuation factor, Q. These important factors are used to be ignored in most forward modeling researches, because they relies on the conventional finite-difference method for its efficiency. Since scattered surface waves are sensitively affected by various geological features and modeling factors, advanced seismic forward modeling approaches should be used for the accurate near-surface modeling. The approach of the spectral-element method with locally-refined hybrid grids in this study shows the capability and potential to handle high impedance contrast boundaries for the analysis of interaction between the seismic wave scattering and complex heterogeneous shallow media.
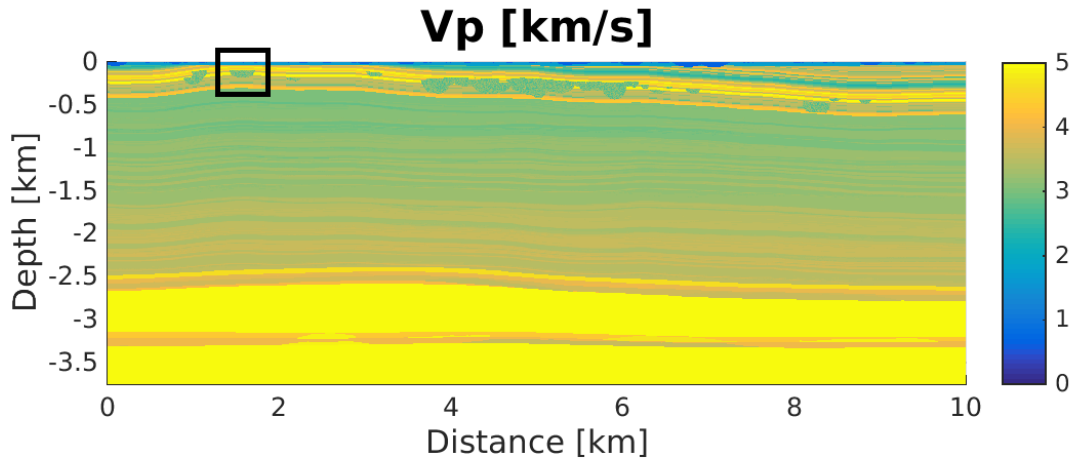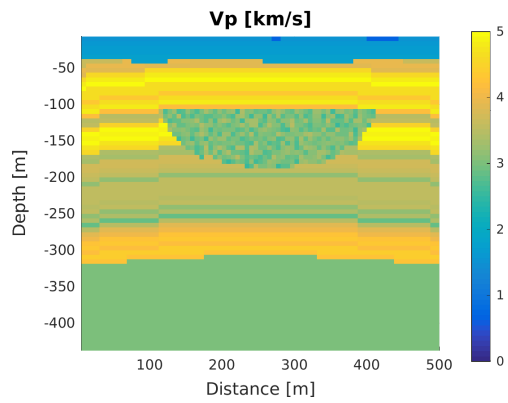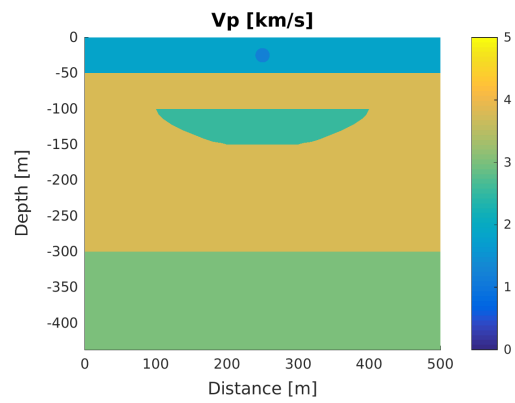
Figure 1.1: Cross section of the benchmark model; SEAM 2 project "arid model". (a) whole size of the geology model data $(10km \times 3.75km)$, (b) only small scale part $(500m \times 450m)$ from the black box of Figure (a), and (c) simplified model to focus on near-surface anomalies: a small size shallow scatterer, a buried collapsed filled karst structure, and a low-velocity top layer.

2. METHOD: SPECTRAL-ELEMENT METHOD AND MESH GENERATION

2.1   Spectral-Element Method

The spectral-element method is based on a weak formulation of the wave equation and combines the flexibility of the finite-element method with the accuracy of the pseudo-spectral method (Komatitsch et al., 2005). The discretization of the elements in the wavefield domain is based on high-degree Lagrange interpolation, and integration over each element is accomplished based on the Gauss-Lobatto-Legendre integration(GLL) rule (Komatitsch and Tromp, 1999). Traditional high-order finite-element methods, which use Gauss-Legendre integration, have suffered from expensive computational costs. However, this approach using the spectral-element method leads to an exactly diagonal mass matrix. Therefore, the algorithm can be drastically simplified in matrix inversion calculation.

In geophysics, the most widely used approach for seismic wave propagation forward modeling was the finite-difference method (Kelly et al., 1976). Although the finite-element method has obvious advantages based on flexible meshes for complex geological structures, its accuracy was lacking. To overcome this problem, the pseudo-spectral method was proposed. This approach is highly accurate, but it cannot handle the complex geometries in the earth model. The spectral-element method was first announced in the field of fluid dynamics (Patera, 1984). This method combines the advantages of both the finite-element and the pseudo-spectral methods. Thus, it can handle complex geometries with great accuracy. This approach was first used in geophysics in 1991 (Seriani and Priolo, 1991). Based on this study, many geological applications in not only 2-dimensions (Komatitsch et al., 2000; Komatitsch and Tromp, 2003; Liu et al., 2012) but also 3-dimensions have been published (Galvez

et al., 2014; Komatitsch and Vilotte, 1998; Lee et al., 2008).

The spectral-element method has caused great interest in computational seismology because the exact diagonal mass matrix leads to a simple explicit time scheme, and it is effective for parallel implementation. Furthermore, notable improvement for near-surface modeling was developed in 2002 (Komatitsch and Tromp, 2002a). The 3-dimensional heterogeneous earth models were implemented, including topography, attenuation and even anisotropy (Komatitsch and Tromp, 2002b). These were challenging topics in conventional finite-difference methods, but they were inevitable factors to overcome in near-surface modeling. The accuracy of the new spectral-element method was compared to the traditional finite-element method and the analytical solution for the wave equation (De Basabe and Sen, 2007). The spectral-element method has been used for various research topics in geophysics (Galvez et al., 2014; Luo et al., 2009), and the development of this approach is still in progress.

In this study of seismic wave propagation, an open source software package, SPECFEM2D (*http://geodynamics.org/cig/software/specfem2d*), which is based on the spectral-element method is used. The software can simulate forward and adjoint seismic wave propagation in 2D acoustic, elastic, poroelastic or coupled acoustic-elastic media, with convolution PML absorbing conditions. The SPECFEM2D package was first developed by Dimitri Komatitsch and Jean-Pierre Vilotte at IPG in Paris (France) from 1995 to 1997. Since then, it has been developed and maintained by CIG seismology group (*http://geodynamics.org/cig/working-groups/seismology*), and the code is released open-source under the CeCILL version 2 liceense. Among their various software packages, this SPECFEM2D package considers 2-D SH and P-SV wave propagation, and the solver can run both in serial and in parallel. All SPECFEM2D software is written in Fortran2003 with full portability in mind, and conforms strictly to the Fortran2003 standard. The package uses parallel program-

ming based upon the Message Passing Interface (MPI), and the next release of the code will include support for GPU graphics card acceleration.

2.2   Mesh Generation Tool CUBIT

Since shallow velocity anomalies usually have low-velocity material properties, extremely fine grids are an indispensable part of near-surface modeling. The mesh scheme as locally-refined quadrilateral hybrid grids is adopted in this study to reflect these geological conditions of the near-surface model. A hybrid grid means a combination of uniform square-shaped structured grids and partially unstructured quadrilateral grids. Unstructured fine grids are applied to only the shallow part. On the other hand, the relatively less complex deep part has traditional regular Cartesian grids.

Even though the advantage of the unstructured grids, mesh generation usually requires expert techniques and takes a large amount of work. To overcome this problem, a mesh generation software program CUBIT (Sandia Laboratory, *http://cubit.sandia.gov*) has been used. The benefit of this tool for the spectral-element method in seismology simulation was proven in the paper (Casarotti et al., 2008). I developed a MATLAB code to arrange complex CUBIT mesh data, and extract 2-D cross section to apply the locally-refined hybrid grids to SPECFEM2D. This approach drastically reduces the total number of elements in the entire model. Thus, the total simulation running time can be also decreased. Since these hybrid grids contain regular Cartesian grids at the deep part, traditional modeling input data format in geophysics field (SEG-Y format data) can be applied easily. Therefore, the potential possibility of this locally-refined hybrid grids approach needs to be considered for near-surface modeling.
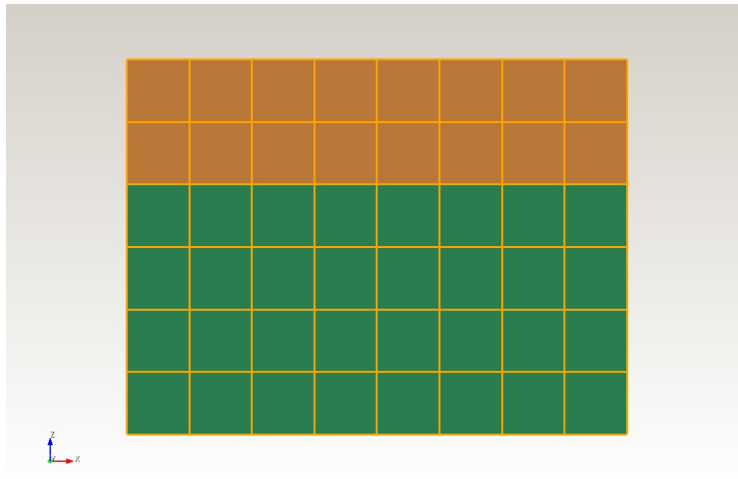
(a)
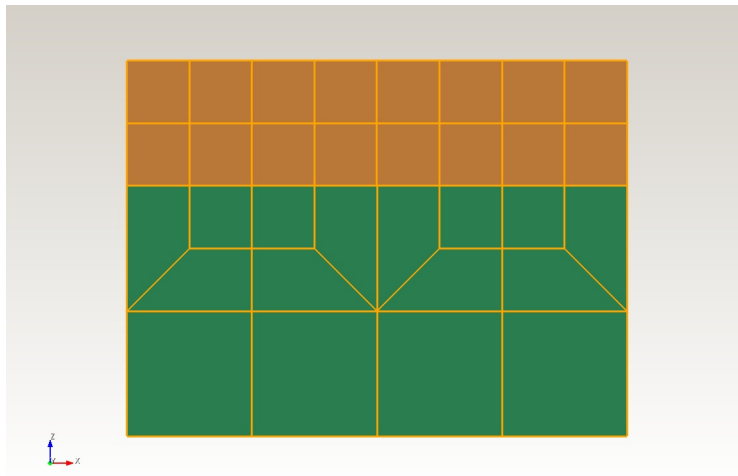
(b)

Figure 2.1: Comparison between the regular grid and locally-refined hybrid grids. (a) traditional uniform fine grid. (b) locally-refined hybrid grids. The near-surface layer (orange) has finer grid than the deep layer (green).

3. MODELING TESTS: NEAR-SURFACE MODELS

3.1 Simple Near-Surface Modeling

To analyze the seismic effects from near-surface velocity anomalies, simplified synthetic earth model (Figure 3.1) is made by CUBIT software. The anomalies are three near-surface geological features: the low-velocity top layer, a shallow small circular shape scatterer, and a collapsed karst structure. The depth of the karst structure is between $100m \sim 150m$, and the length of the upper boundary is $300m$. The semi-circle shapes on its left and right sides represent the features of collapsed subsurface karst structures (Metwaly and Alfouzan, 2013). On the other hand, the shallow scatterer has a $10m$ radius perfect circle shape. This ideal assumption can be different from the realistic shape of shallow anomalies, but circular geometry is applied as a first step of the shallow anomalies' complex geometry. The center of the scatterer is located in the middle part ($250m$, $25m$), and the distance between the free-surface and the scatterer upper boundary is only $15m$.
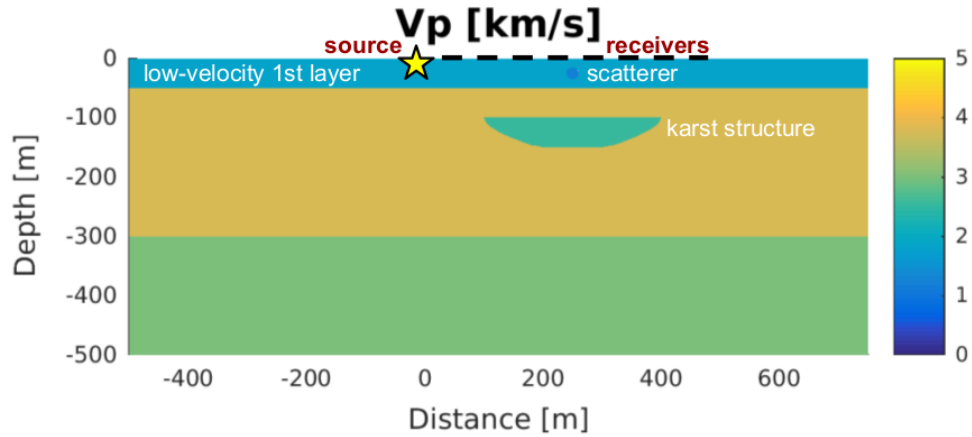
Figure 3.1: Simple synthetic near-surface model

9

Table 3.1: Material properties and modeling parameters of the simple synthetic near-surface earth model in Figure 3.1.

Material Layers	Depth (m)	Vp (km/s)	Vs (km/s)	Shortest wavelength (m)	Grid size (m)
1st layer	$0 \sim 50$	1.8	1.0	16.7	2
2nd layer	$50 \sim 300$	3.8	2.1	35.0	4
3rd layer	$300 \sim 500$	3.0	1.7	28.3	4
scatterer	$15 \sim 35$	0.8	0.4	6.7	1
karst structure	$100 \sim 150$	2.5	1.4	23.3	4

As I mentioned in the introduction chapter, all the geometry and material properties of near-surface velocity anomalies are based on the official released data "arid model" of the SEAM 2 project, and detail values of material properties are shown in Table 3.1. The most challenging part is that the minimum velocity is only 0.4 km/s inside the scatterer. Since the spectral-element method modelings use high-order basis functions, I decided to use 1 m grid spacing, so the number of elements in the shortest wavelength is about 6. The unstructured grids, generated by CUBIT software, changes the grid size gradually from $1m$ to $4m$.

Simple earth models with only one anomaly, the karst structure model (Figure 3.2-a) and the scatterer model (Figure 3.2-b), are developed to identify the wave propagations. These anomalies are filled with low-velocity materials, so the distortions of wave propagation from them are shown in snapshots (Figure 3.2-c & d). S-wave and surface wave (Rayleigh wave) propagation is captured at time 0.3 sec.

The first snapshot (Figure 3.2-c) from the karst structure model shows a distorted S-wave because of the subsurface karst structure. The S-wave propagation in this low-velocity anomaly is obviously slower than the surface wave, and the semi-circle shape on the right side of the karst structure boundary reflects the S-wave strongly. This can be used to infer the location of subsurface karst structures in the seis-
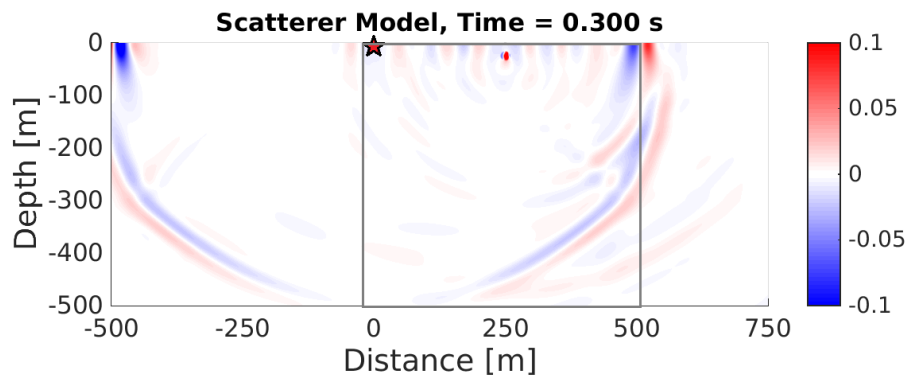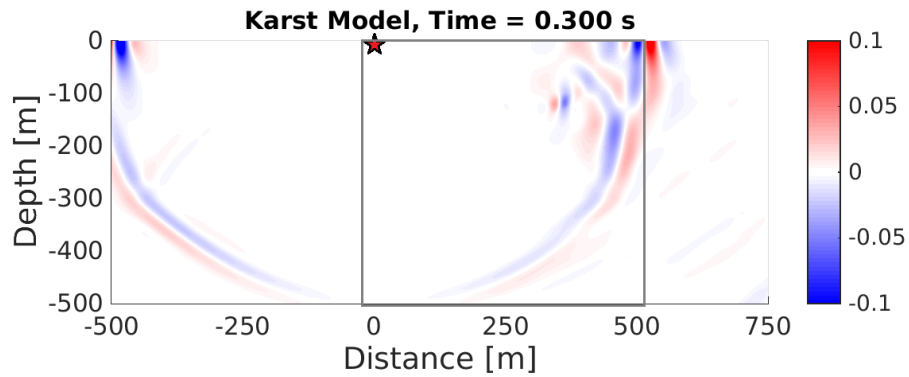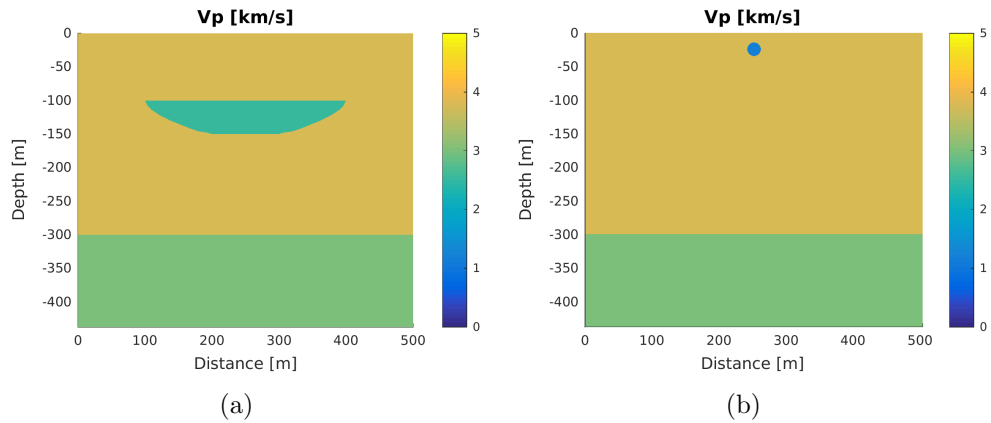
Figure 3.2: Snapshots of wave propagation in simple near-surface models. (a) karst model, (b) scatterer model, (c) snapshot from karst model, and (d) snapshot from scatterer model. The snapshots show vertical component of each point displacement, and the obvious circular waves at 0.3 s are S-waves. The red star shows the location of source at the surface (0 m , 0 m), and the grey rectangular box shows the size of each synthetic model. Wide range of x-axis distance is used to ignore the artificial reflections from the left and right boundaries.

mogram. The scatterer, filled with extremely low-velocity materials, shows strong seismic energy trapped in it (Figure 3.2-d). The reason for this high amplitude is the strong direct surface wave whose amplitude decreases exponentially with increasing depth. Since the depth of the scatterer is shallow, we can see the strongest seismic energy in this snapshot. This trapped energy generates continuous forward and back-scattered surface waves, and it corrupts the seismic data quality. This signal contamination used to be simply erased and ignored as ground roll in traditional seismic data processing. However, the amplitude and propagation patterns of scattered waves should be carefully analyzed in modeling, because this can be used for surface wave inversion to distinguish noise from scattered waves by upcoming P-waves.

3.1.1   Difference between regular Cartesian grids and locally-refined hybrid grids

Based on the analysis of seismic wave propagation in simple earth models, I compared the difference between regular Cartesian grids and locally-refined hybrid grids on the same synthetic near-surface model (Figure 3.1). The shapes of these two grid schemes on the same material base synthetic near-surface model are shown in Figure 3.3. The figures are focused around the shallow circular scatterer, which has the most complex geometry of material boundary in a simple near-surface model, and the karst structure boundaries are drawn by the same grid schemes. Because of extreme low-velocity material in the scatterer, the cell size of a regular Cartesian grid (Figure 3.3-a) is only 1 m in both x & z axis. However, locally-refined unstructured grids (Figure 3.3-b) show various cell sizes from $1\ m$ in the circular scatterer to $4\ m$ in the deep part. The colorbar of figures shows the material velocity properties, and the structured grid in the deep part is fine enough to prevent the artificial dispersion errors because of relatively high velocity material properties. The unstructured grids
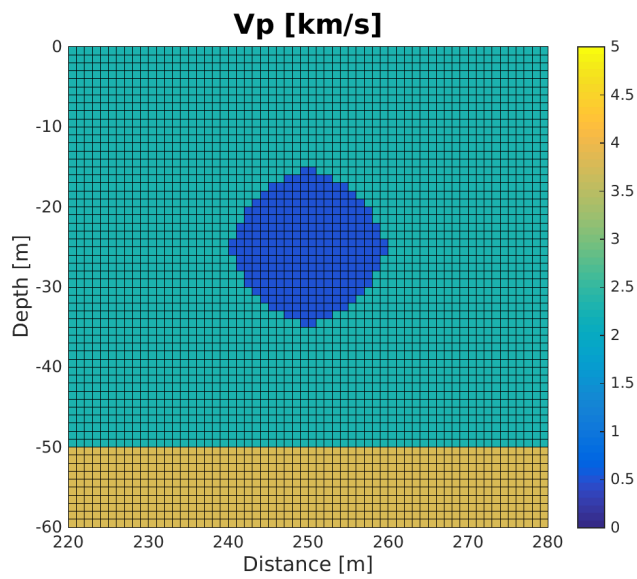
(a)
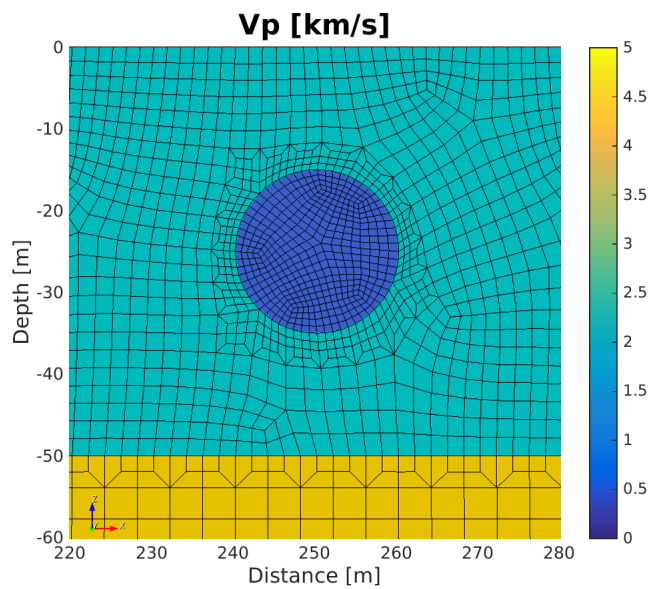
(b)

Figure 3.3: Two different grids near the shallow small circular scatterer in the simple synthetic earth model (Figure 3.1). (a) regular Cartesian grid, (b) locally refined hybrid grid. Figure (b) shows more smooth curved material boundary around the scatterer.

can change the grid size to use fewer numbers of elements in the model, and it can also represent a much smoother material boundary of the circular scatterer. The irregular shape of unstructured grids around the velocity anomalies can generate conforming mesh on the curved line smoothly without any sharp edges. When we use regular Cartesian grids, the curved line of material boundaries should be drawn with artificial sharp edges of 90-degree angles. This used to be ignored for large scale structures, but near-surface models have to consider small scale anomalies that are sensitive to grid shape.

Since we analyzed the wave propagation in the simple karst model and scatterer model in previous chapter, these two models are used again to compare different modeling grid designs. The Figure 3.4 shows the differences in results between two different grid schemes in karst structure models (Figure 3.2-a). From left to right, the synthetic seismogram shows the result from regular Cartesian grids, locally-refined unstructured grids and the difference between them by data subtraction. The seismogram from the karst structure model shows almost same result. The most different signals in Figure 3.4-c are the artificial reflections at the end (time 0.52 s) from non-perfect absorbing boundary conditions in the unstructured grid model. Apart from that difference, most of the other signals are the same, because the geometry of the karst structure is relatively simple, and the length and height of this structure is much longer than the seismic wavelength.

However, the resulting seismogram from the scatterer models (Figure 3.2-b) show a notable difference between the two different grid models. The seismogram from the regular Cartesian grids (Figure 3.5-a) and locally-refined unstructured grids (Figure 3.5-b) seem almost the same, but the difference between them (Figure 3.5-c) shows various amplitude and propagation patterns of multiple scattered surface waves. To be specific, the amplitude of first scattered waves from the direct surface wave is

14
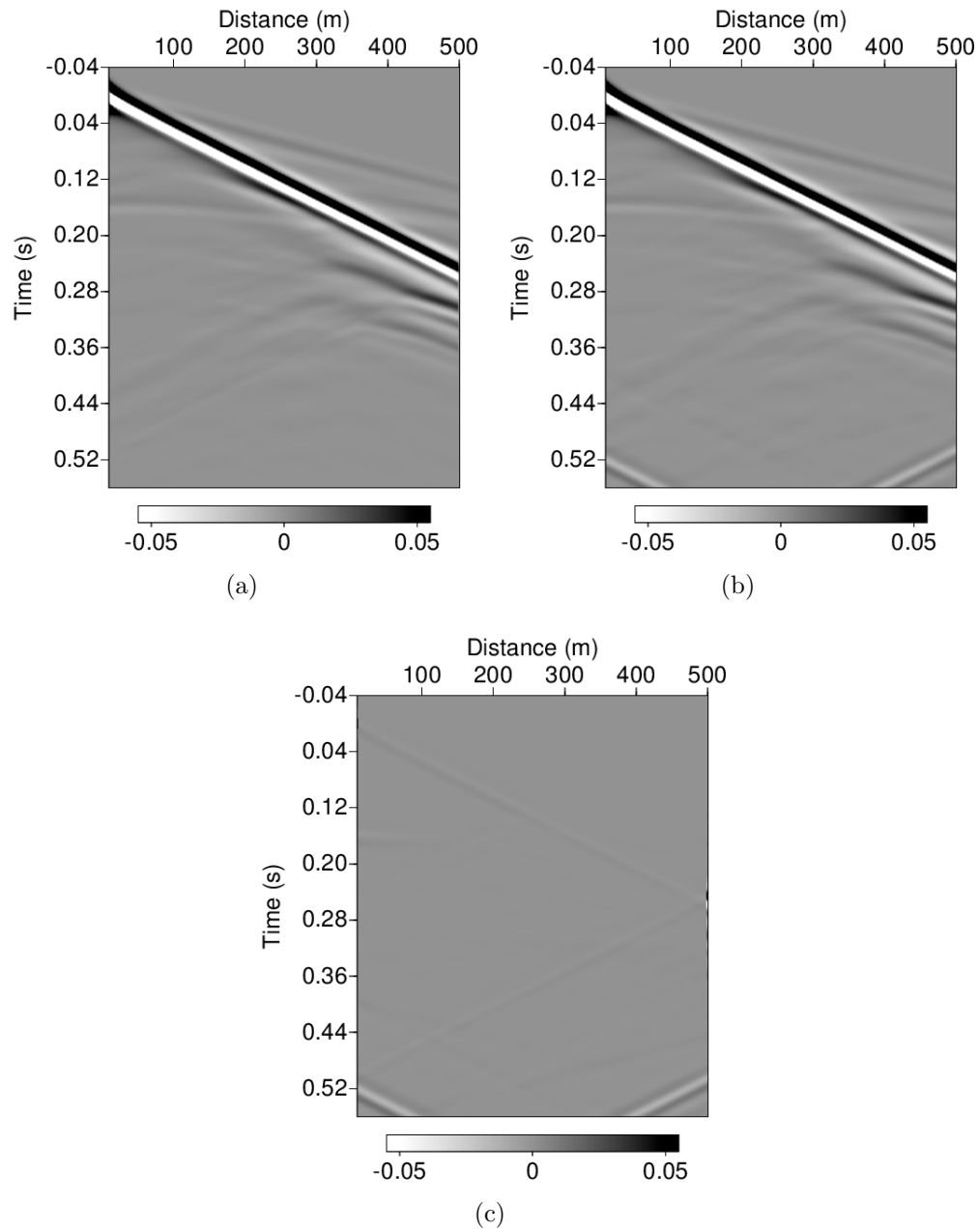
Figure 3.4: Synthetic seismograms with different grids in the karst model.(a) regular grid karst model, (b) hybrid grid karst model, (c) the difference between (a) & (b). The grid shows few difference because the karst structure size is relatively bigger than the grid spacing.
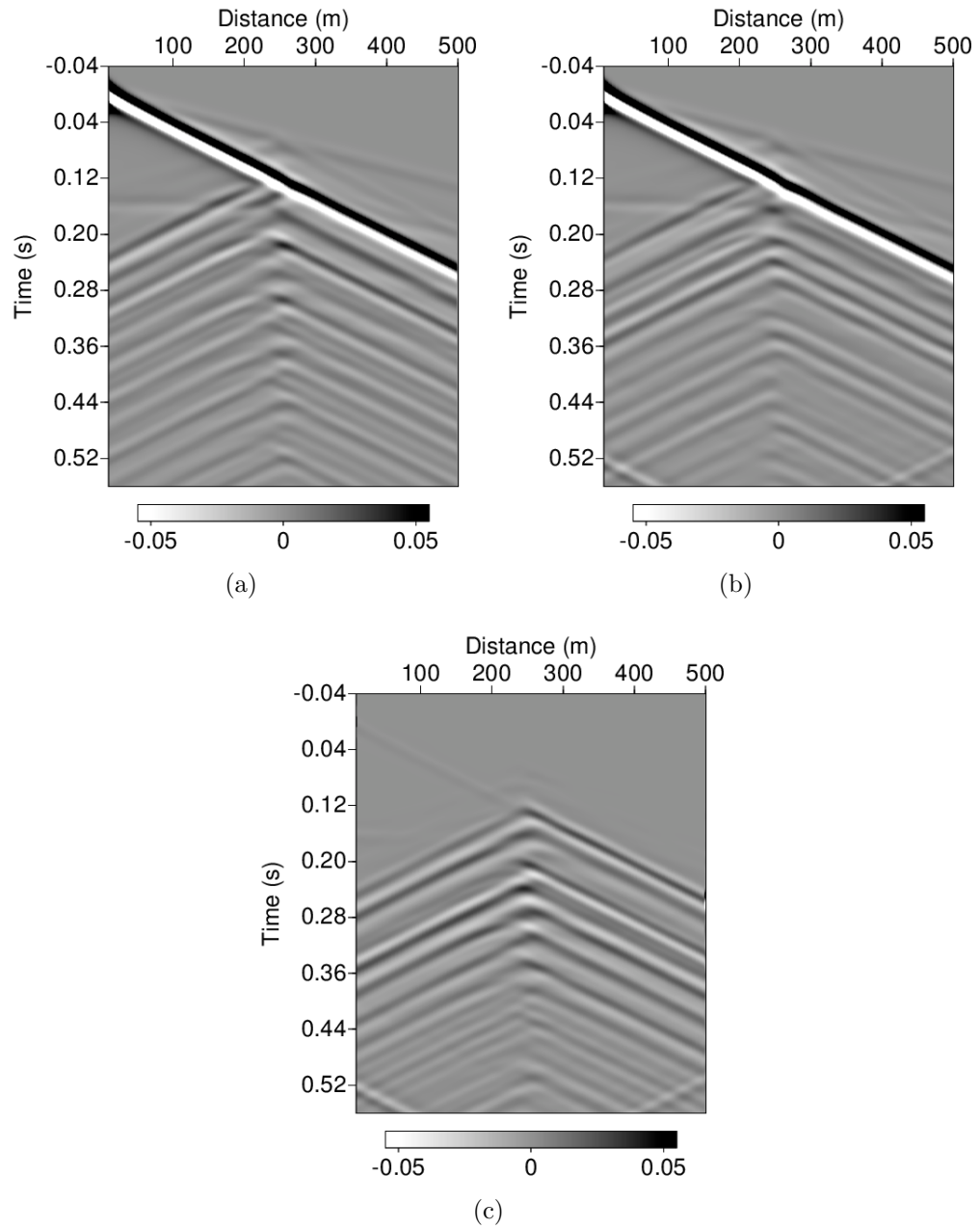
Figure 3.5: Synthetic seismograms with different grids in the scatterer model.(a) regular grid scatterer model, (b) hybrid grid scatterer model, (c) the difference between (a) & (b). The difference of grids shows the different signals. The amplitude of scattered surface wave is affected by the shape of grid in the small size velocity anomaly.

different, and the regular Cartesian grid model shows stronger backward scattered waves. Otherwise, the amplitude of multiple scattered waves from trapped seismic energy in the scatterer is weaker than that of the unstructured grid model. Since grids are generated based on at least five cells per the shortest wavelength, this difference cannot be defined as artificial dispersion errors from the coarse grid in the spectral-element simulation with unstructured grids. This shows that the shape of modeling grids causes the different geometry of small scale velocity anomalies, and this decreases the accuracy of near-surface modeling. This seems a small difference, but we can predict a significant difference in surface wave inversion, which we should consider carefully with the wave amplitude with attenuation factor.

3.1.2 Effect of materials in scatterer

In the previous chapter, we found that the low-velocity solid scatterer generates multiple scattered surface waves. However, this small size scatterer may be filled with various kinds of materials in real arid karst areas. A case study (Peters et al., 1990) shows that the shallow karst regions in Saudi Arabia contain various near-surface anomalies that are filled with low-velocity sediments or water. Air-filled small cavities or large caves are also found in these karst areas in shallow weathered layers.

To compare and analyze the seismic effect difference due to the materials inside the scatterer, three types of additional scatterer models are used. These have the same geometry as the previous low-velocity solid scatterer model of Figure 3.2-b, but the inside materials are high-velocity solid, water, and air. In these models, the upper layer material P-wave velocity is 3.8 km/s, the same property of the high-velocity scatterer is 5.0 km/s, and the Vp of water and air cases are each 1.5 km/s and only

0.3 km/s. Since water and air are acoustic material, S-wave velocity is applied to only solid materials as $Vp/1.8$. The density of water is 1.0 g/cm^3, but air density is assumed to be extremely low at 0.001 g/cm^3.

The resulting seismograms from these three difference scatterer models are compared in Figure 3.6. From left to right, results are generated from the high-velocity solid-filled scatterer, low-velocity solid-filled scatterer the same as Figure 3.5-b, water-filled cavity and air-filled cavity. The first result (Figure 3.6-a) is the simplest, because the high-velocity scatterer does not trap seismic energy. The scatterer causes only simple scattering from the direct surface wave. However, the water-filled cavity case (Figure 3.6-c) shows faint multiple scattered surface waves from trapped energy in the water-filled cavity. Their amplitude is obviously weaker than the result from the low-velocity scatterer model (Figure 3.6-b). The notable difference between the low-velocity scatterer model and the water-filled cavity model is not only the amplitude of waves, but also the time intervals of multiple scattered surface waves from the scatterer. The time interval of regenerated scattered surface waves in the low-velocity solid scatterer model is about 0.04 s, but the water-filled cavity case shows about 0.02 s, which is only half of the previous result. Since water contains only P-wave energy, which is weaker and faster than that of surface wave energy, scattered surface waves as multiples has a fast velocity, and the interval time between multiples become shorter. We can say that, the scattering surface waves by upcoming P-waves, which is very important to identify hydrocarbon reservoirs, may present short multiple intervals in seismogram. This time interval difference between surface wave trapped energy and P-wave trapped energy must be considered to do a more accurate surface wave analysis.

The seismogram of the air-filled cavity model (Figure 3.6-d) is also different from the water-filled case (Figure 3.6-c). Air-filled cavity cases were regarded the same as
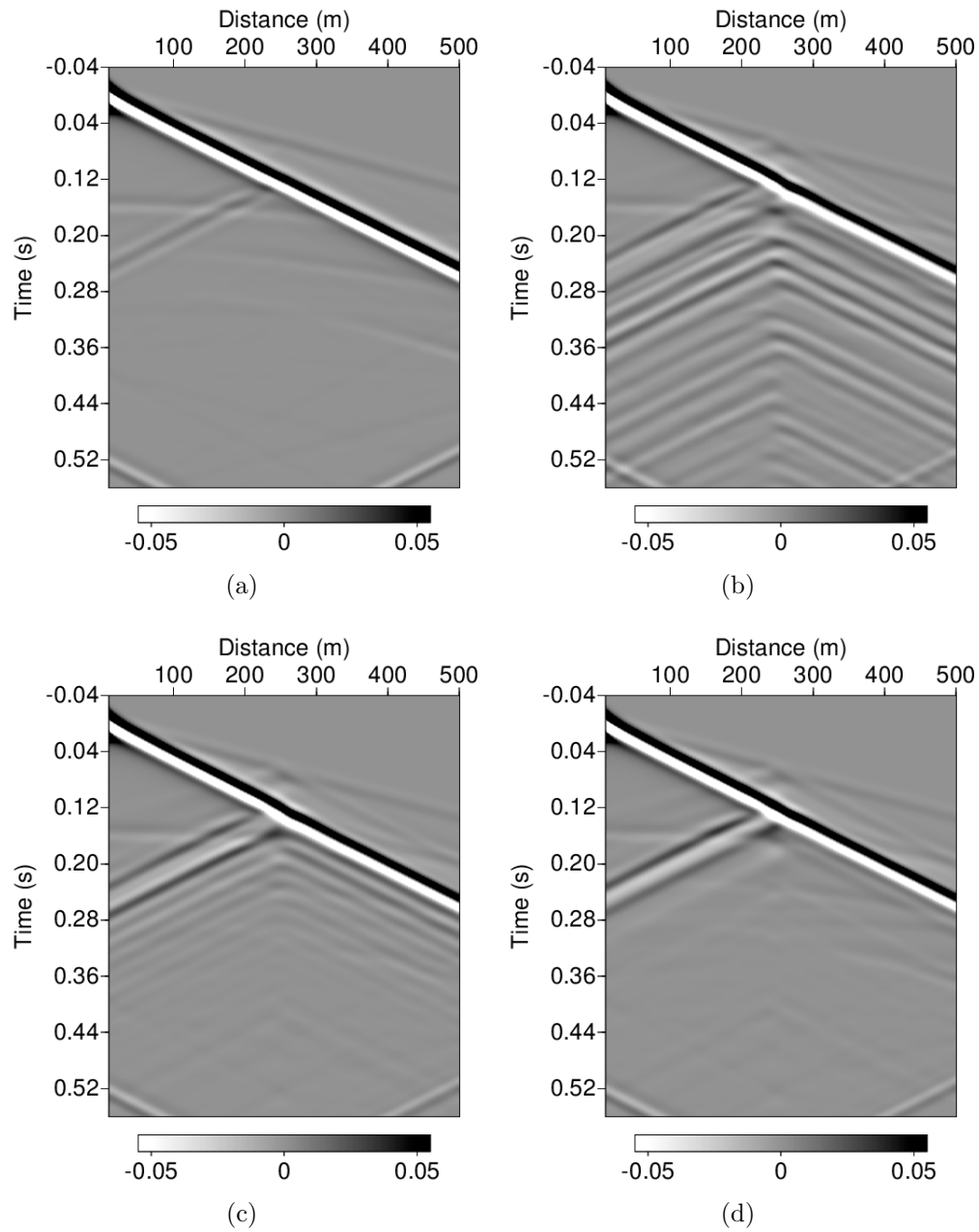
Figure 3.6: Synthetic seismograms from scatterer models with different filling materials. (a) high-velocity solid-filled scatterer, (b) low-velocity solid-filled scatterer is the same as Figure 3.5-b , (c) water-filled scatterer, (d) air-filled cavity. The scattered surface waves are different due to the materials in scatterer.

19

water-filled cavity cases in the past (Oristaglio, 2012). However, the air-filled cavity doesn't generate multiple wave noises from trapped seismic energy. We can only find rare scattered surface waves, which come from upcoming reflected P & S waves. The air-filled cavity result is similar to the high-velocity solidd scatterer simulation rather than water-filled cavity simulation.

To clarify the seismic waves inside these challenging water-filled and air-filled cavity, I compared snapshots of the seismic wave propagation inside the cavities. Two different types of snapshot for each case were used. One type was a horizontal X-component displacement snapshot, and the other type was a vertical Z-component displacement snapshot. These two different snapshots were useful to analyze both transverse waves and longitudinal waves. The trapped seismic waves inside the air-filled cavity showed both X & Z components. This energy came from the direct surface waves, but it didn't penetrate the boundary of the cavity. However, the waves inside the water-filled cavity were different. The transverse waves were obviously converted into longitudinal waves in the water, and those strong waves regenerated seismic scattered waves to the outside of the cavity. This noise was related not only to the seismic energy inside the cavity but also to the boundary waves around the circular cavity. These waves are complex, but it supports the previous discussion that P-wave energy affects mainly the scattered seismic noise from the water-filled cavities.

The seismogram results show different amounts of trapped seismic energy inside the scatterer, and the scattered noise waves are strongly dependent on the materials inside the scatterer. This demonstrates that if we could distinguish multiple scattered surface waves based on an accurate near-surface modeling, then it would be possible to erase the noise successfully in seismic data processing and improve the inversion for P-wave imaging of deep structures.

3.1.3   Effect of attenuation

To identify the multiple scattered surface waves from the trapped energy in low-velocity anomalies correctly, attenuation should be considered in forward modelings. The attenuation factor Q is theoretically defined in seismology (Aki and Richards, 2002) to identify the amount of decreasing amplitude with ray path distance increasing in wave propagation.

$$\frac{1}{Q(w)} = -\frac{\Delta E}{2\pi E} \tag{3.1}$$

where E is the peak strain energy, $-\Delta E$ is the energy loss per cycle and Q is sometimes called the $quality\,factor$. Since this Q is inversely related to the strength of the attenuation, low-Q value means more attenuating regions than high-Q. In general seismology, the energy loss per cycle is very small and amplitude can be derived as in the following approximation.

$$A(x) = A_0 e^{\frac{-wx}{2cQ}} \tag{3.2}$$

where x is measured along the propagation direction and c is the wave velocity. If $c = \alpha$ for P waves, Q_α is used for attenuation, and if $c = \beta$ for S waves then Q_β is used. The amplitude $A(x)$ of harmonic waves may be written as a product of a real exponential of amplitude decay due to attenuation and an imaginary exponential describing the oscillations (Shearer, 1999).

This Q factor has been developed and applied in spectral-element method modeling (Komatitsch and Tromp, 2002a,b), so the simple low-velocity scatterer model, which has the strongest trapped energy, is used again with the attenuation Q fac-
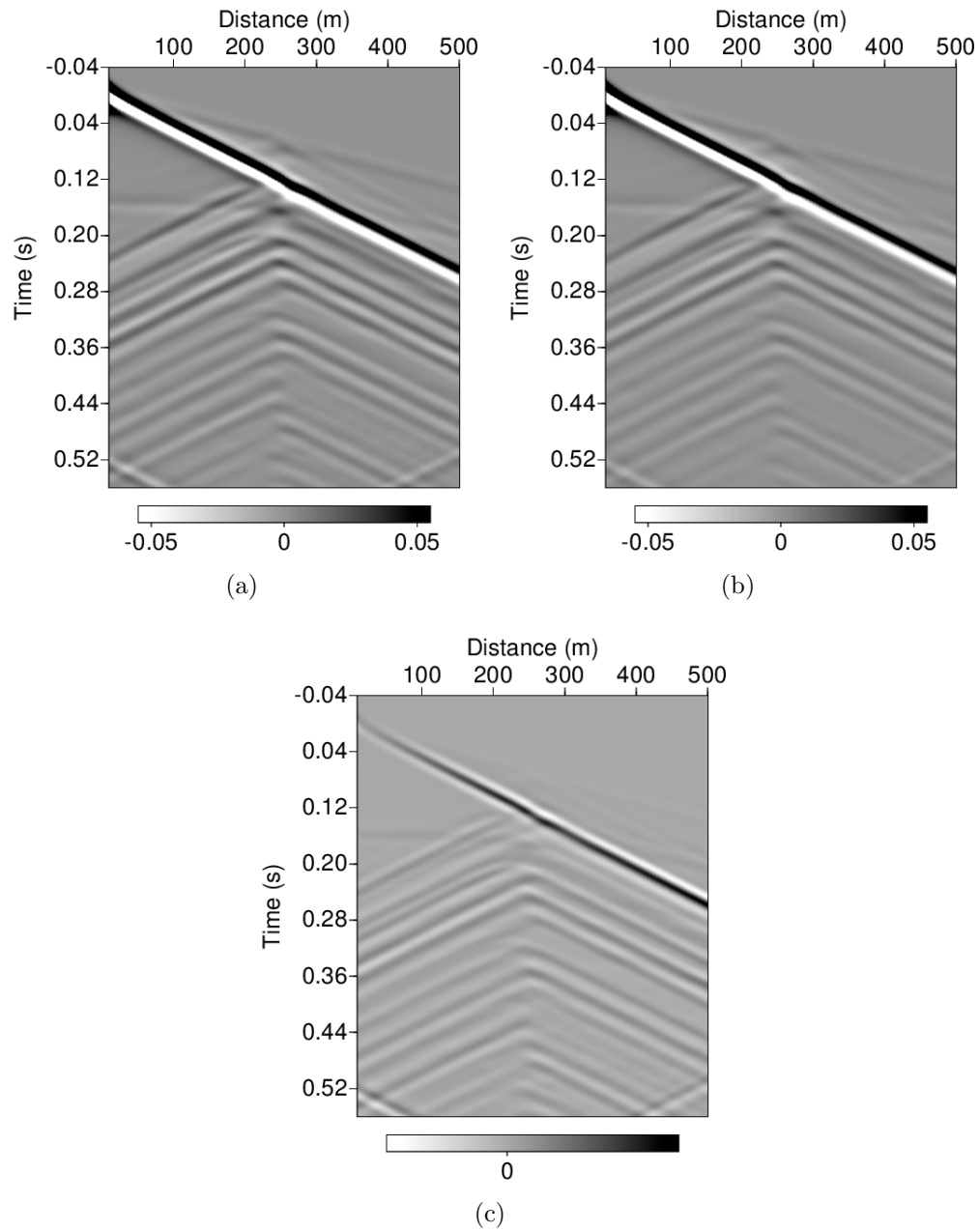
Figure 3.7: Synthetic seismograms of low-velocity material scatterer models with different attenuation conditions. (a) No attenuation, (b) attenuation Q factor = 100. (c) the difference between (a) & (b). The scattered surface wave amplitude is strongly affected by the attenuation factor.

tor. The result of these modelings are presented in Figure 3.7. From left to right, seismograms are obtained from non-attenuation modeling (Q = 9999), attenuation modeling (Q = 100), and the difference between two results by subtraction. The difference (Figure 3.7-c) shows that amplitude of direct surface wave is decreased as offset distance from source location increase, and the amplitude of multiples in Figure 3.7-b is less than Figure 3.7-a. This indicates that attenuation in synthetic forward modeling is important to compare results with field data for sensitive scattered surface waves analysis.

3.1.4   Effect of topography

The most notable benefit of using the spectral-element method modeling is the flexibility in applying complex free-surface topography. Since surface waves strongly depend on the condition of free-surface, many approaches in conventional finite-difference have been developed for topography (Appelo and Petersson, 2009; Bohlen and Saenger, 2006; Robertsson, 1996; Tessmer et al., 1992). I developed new karst structure model (Figure 3.8-d) and the scatterer model(Figure 3.9-d) including the Gaussian curved shape of free-surface topography. I compared these with previous flat free-surface model results to show how these challenging near-surface factors affect scattered surface waves.

Two different receiver locations are used. From left to right, the seismograms in Figure 3.8 and Figure 3.9 show the seismogram from the curved free-surface model with a constant receiver line elevation ($z = 0m$), and the curved free-surface model with a constant receiver line depth ($d = 10m$) offset from Gaussian curved free-surface geometry, the flat free-surface topography model as reference and the geometry of earth model. The surface receiver line elevation is constant as $0m$ in Figure

23
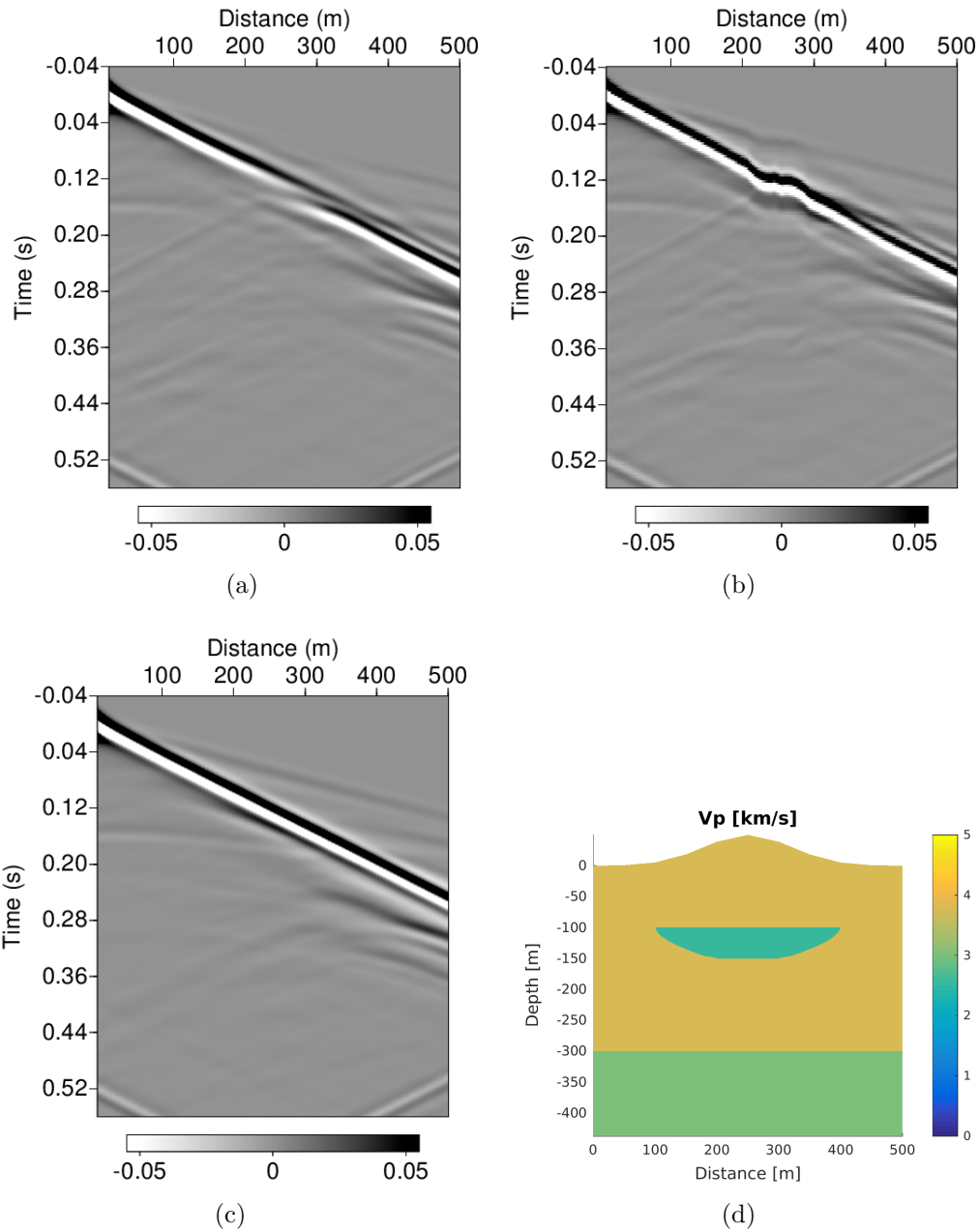
Figure 3.8: Synthetic seismograms from karst models with topography. (a) curved free-surface karst model with flat receiver line, (b) curved free-surface karst model with conforming receiver line, (c) flat free-surface karst model as reference, (d) sketch of the curved free-surface karst model. Irregular topography can be inferred from the shape of direct surface waves. Furthermore, the hill also induces the scattered backward surface wave propagation.
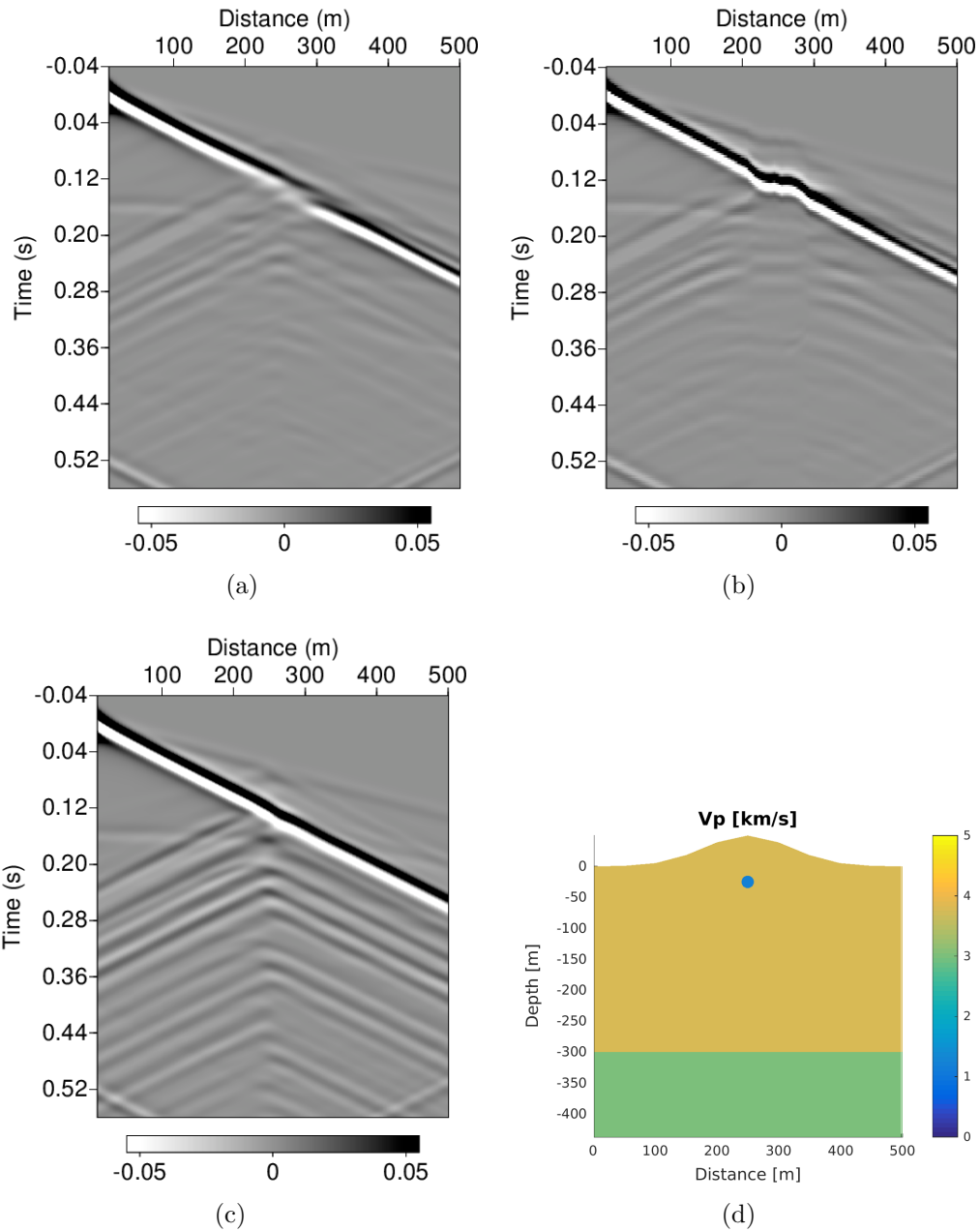
Figure 3.9: Synthetic seismograms from scatterer models with topography. (a) curved free-surface scatterer model with flat receiver line, (b) curved free-surface scatterer model with conforming receiver line, (c) flat free-surface scatterer model as reference, (d) sketch of the curved free-surface scatterer model. Since the hill decrease the amplitude of surface waves at shallow scatterer, the trapped seismic energy is much smaller than that of the flat free-surface model. Thus, scattered surface wave noises in (a) & (b) are much smaller than (c).

3.8-a & Figure 3.9-a. That means that only a few receivers in the middle part are buried in the dune under the free-surface. Otherwise, all receivers in Figure 3.8-b & Figure 3.9-b are buried at a constant depth $10m$ from the curved free-surface. As we can see in seismograms, shape of the direct surface waves are different. The former cases have discontinued surface wave line, and latter cases have continuous line with a distorted flat part at the middle. These obvious changes of direct surface wave line due to the different receivers location lead us to easily predict the effect of free-surface topography, and this can be used for interpretation in the next step.

The evidence of topography in seismogram is important to analyze scattered surface waves from velocity anomalies. In the karst model seismogram (Figure 3.8-a & b), there is another backward scattered surface waves due to the surface dune. The karst structure model does not include the shallow scatterer, and the first layer of this model is even homogeneous. The backward scattered surface wave can be misunderstood to image an accurate near-surface model, and this wave shows the reason why we have to use accurate unstructured grid forward modeling to handle the surface topography.

The topography hill also causes a big effect on the trapped seismic energy inside the shallow scatterer. The figure 3.9 shows significant different amplitude of multiple scattered waves. Since the trapped seismic energy in the shallow scatterer strongly depends on the direct surface wave, increasing the height of the topography of the dune decreases the surface wave amplitude. Consequently, less energy is trapped in the velocity anomaly, and scattered surface waves become weaker. Since the ultimate goal of this study is the accurate surface wave analysis and inversion to improve P-wave imaging, even a tiny difference of scattered surface waves should be carefully understood.

3.1.5 Effect of low-velocity top layer

Although many factors have been discussed to analyze each effect in the seismogram, the low-velocity top layer must be the most difficult factor because of surface wave dispersion. Wave dispersion refers to frequency dispersion, which means that waves of different wavelengths travel at different phase velocities. Because of the low-velocity top layer, a lot of seismic energy is trapped, and it causes severe surface wave dispersion. Since the amplitude of the surface wave is larger than that of other waves, dispersed surface has been used to explore shallow layers in engineerings (Almalki and Munir, 2013; Park et al., 1999; Xia et al., 1999). Previous studies used Rayleigh wave dispersion to find subsurface S-wave velocity properties or to detect near-surface cavities. This approach has the potential possibility to improve not only near-surface surface wave inversion, but also obscure scattered surface waves, which come from reflected P & S waves from deep target structures.

As the first step for challenging surface wave dispersion analysis, a seismogram (Figure 3.10-a) from a simple 3 layered earth model including the low-velocity top layer, is analyzed. The velocity anomalies are ignored, so the seismogram shows only simple reflections and dispersion. Even though this simple model has only three horizontal layers, the seismic data signal quality is poor because of strong surface wave dispersion. Unfortunately, the seismogram shows some multiple backward scattered surface waves from the middle of the earth model. These noise signals are artifacts caused by the changing cell size and geometry in the unstructured grid in the low-velocity top layer. They can be ignored because subtraction of seismograms will eliminate them.

Even though the wave dispersion is severe because of the low-velocity top layer, the karst structure and shallow scatterer as velocity anomalies also show obvious
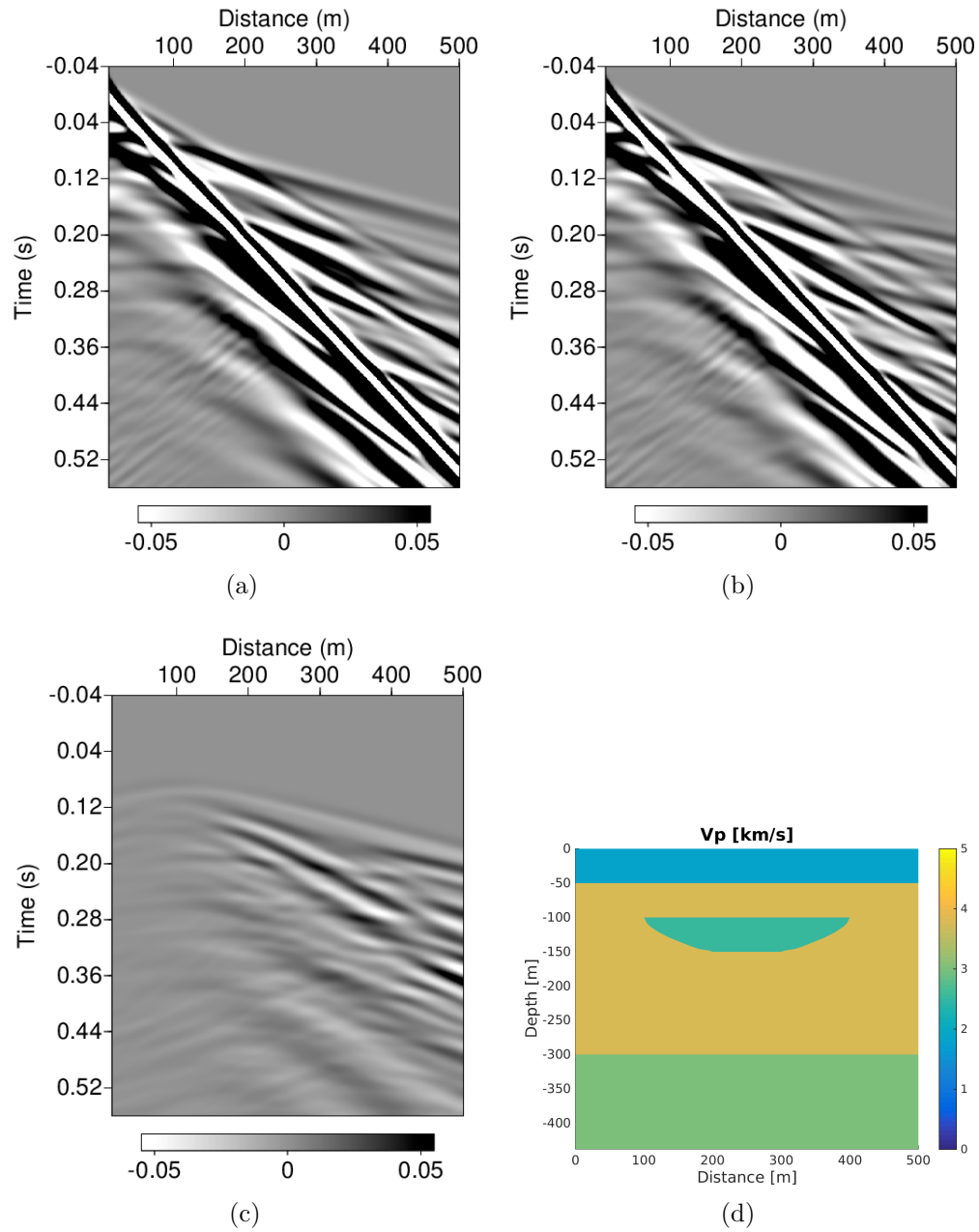
Figure 3.10: Synthetic seismograms from karst models with the low-velocity top layer. (a) result from the karst model without the karst structure as velocity anomaly, (b) result from the karst model of (d), (c) the difference between (a) & (b), (d) sketch of the karst model with the low-velocity top layer. Surface wave dispersion makes signals more complicated, but the signal difference can be found obviously in (c).
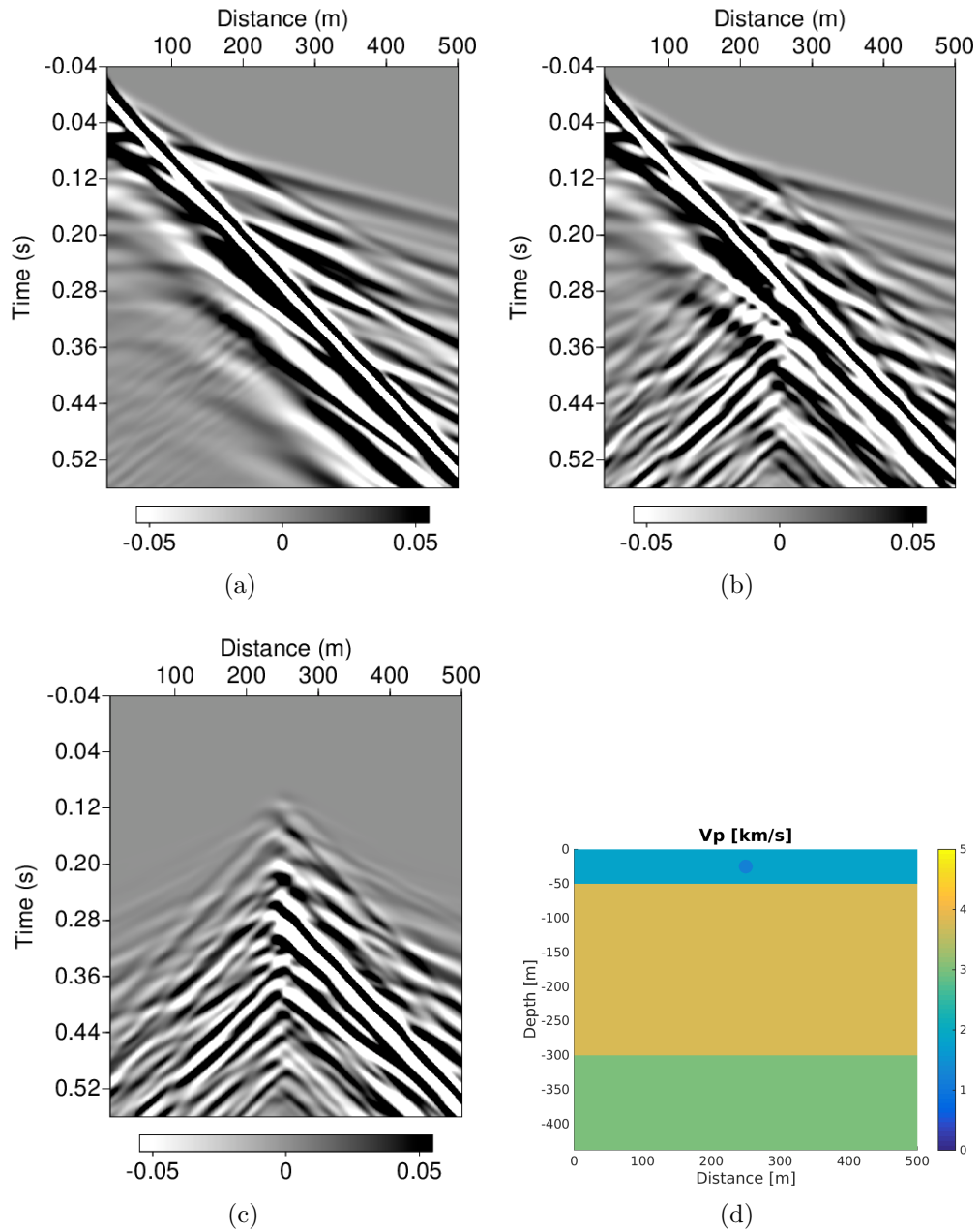
Figure 3.11: Synthetic seismograms from scatterer models with the low-velocity top layer. (a) result from the scatterer model without the scatterer structure as velocity anomaly, (b) result from the scatterer model of (d), (c) the difference between (a) & (b), (d) sketch of the scatterer model with the low-velocity top layer. Surface wave dispersion makes signals more complicated, but the trapped energy in the scatterer is also obvious.

29

differences in the seismograms. Figure 3.10-b is the seismogram with the subsurface karst structure, and Figure 3.10-c is the difference between Figure 3.10-a and Figure 3.10-b. Even though the challenging top layer contaminates the entire signal, the effect of the karst structure can be identified. As we discussed in previous simple near-surface models, the karst structure shows S-wave distortion and reflection from the edge of the karst structure. The scatterer model with the top layer result is more complex. All the dispersed high amplitude surface waves are trapped in this scatterer, and all generate multiple unwanted coherent noises (Figure 3.11-b). Even though we can pick up the only effect from the scatterer in Figure 3.11-c, the multiple scattered surface waves are more complicated than the result from the simple model without the low-velocity top layer (Figure 3.6-b). This shows that surface wave analysis and inversion have to consider this challenging low-velocity top layer in data processing, and we should apply all the factors mentioned above carefully in forward modeling.

3.2   Complex Near-Surface Modeling

The complex near-surface earth model (Figure 3.12) is also developed to clarify the analysis of scattered surface wave propagation. This model includes most of the near-surface anomalies in limestone deserts: the collapsed karst structure, the shallow scatterer, the low-velocity top layer with curved free-surface topography, which we discussed in previous simple modelings. The entire complex model size (x, z) is 1,000 $m \times$ 500 m, and it has 7 horizontal layers with various size of collapsed filled karst structures. The material properties of each layer and anomaly is in the Table 3.2, and the sizes of shallow scatterers are in the Table 3.3.

It was not easy to handle shallow scatterers in seismic forward modeling because of their slowest S-wave velocity as 800 m/s. Because of this material property, the minimum grid spacing should be only 2 m on the near-surface parts of this complex earth model to implement the SPECFEM2D simulation. Since the size of scatterer is very small, another mesh generation software, Gmsh, is used instead of CUBIT. The Gmsh has more benefits in drawing complex geometries of small size anomaly boundaries, and it is convenient to generate unstructured quadrilateral grids. The unstructured grids in the model change the grid size gradually from 2 m to 6 m.

The unstructured grids, generated by Gmsh, could not use effective absorbing boundary conditions in SPECFEM2D forward modeling. Artificial reflections from left and right boundaries corrupts the signal quality, and scattered surface waves due to the shallow scatterer is not obvious. To erase these unwanted noises, the other complex model is developed for the seismogram subtraction. This new complex model has the same geometry and material properties, but it doesn't include 7 shallow small scatterer. These similar complex near-surface models are presented in Figure 3.12. The only Figure 3.12-a includes shallow small scatterers in the middle part of

Table 3.2: Material properties of complex near-surface earth model structures. The units are g/cm³ for density and km/s for P & S-wave velocities. The material minimum velocity property is 0.8 km/s at the shallow scatterers

Layers (from top to bottom)	Density (g/cm^3)	Vp (km/s)	Vs (km/s)
1st	1.95	1.8	1.0
2nd	2.12	2.5	1.4
3rd	2.22	3.0	1.7
4th	2.01	2.0	1.1
5th	2.12	2.5	1.4
6th	2.22	3.0	1.7
7th	2.30	3.5	1.9
shallow scatterers	1.87	1.5	0.8
collapsed karst structure (left)	2.10	2.0	1.1
collapsed karst structure (right)	2.12	2.5	1.4

the 2nd layer, but Figure 3.12-b doesn't have them. Two seismograms from these earth models are compared to extract the only scattered surface waves due to the shallow scatterers. Seismograms are presented in Figure 3.13, Figure 3.14, and Figure 3.15. The 3rd seismogram in each figure is the difference result, which subtracts 2st seismogram from the 1nd seismogram. This subtraction is efficient at analyzing elastic wave scattering from the shallow small scatterers.

Three different source locations (250 m, 500 m, 750 m on the x-axis) are used to see the wave scattering at the middle part of the complex earth model. The 3rd seismogram in each figure, differences between the seismograms with/without the shallow scatterers, shows some yellow polygons on the seismogram to clarify the location of the shallow scatterers. These marks are helpful to find where the scattering begins. Even though the size of shallow scatterers are relatively small, obvious wave scatterings are found from every seismograms. The dominant frequency (f_0) of source Ricker wavelet was $30Hz$, so the shortest wavelength in the 2nd layer should
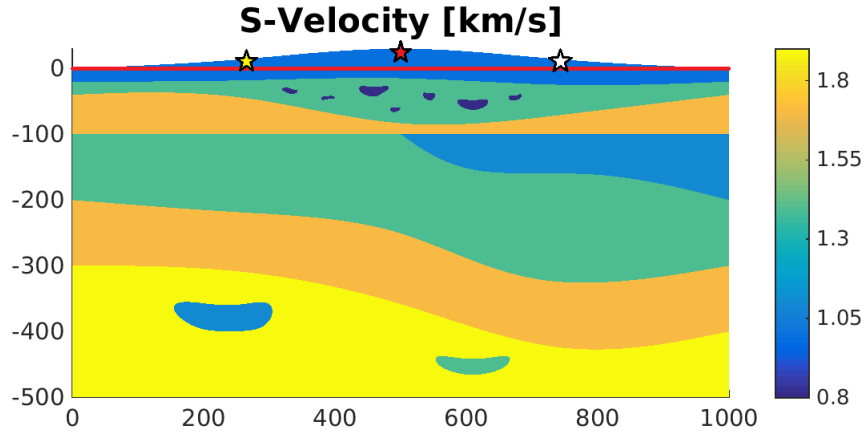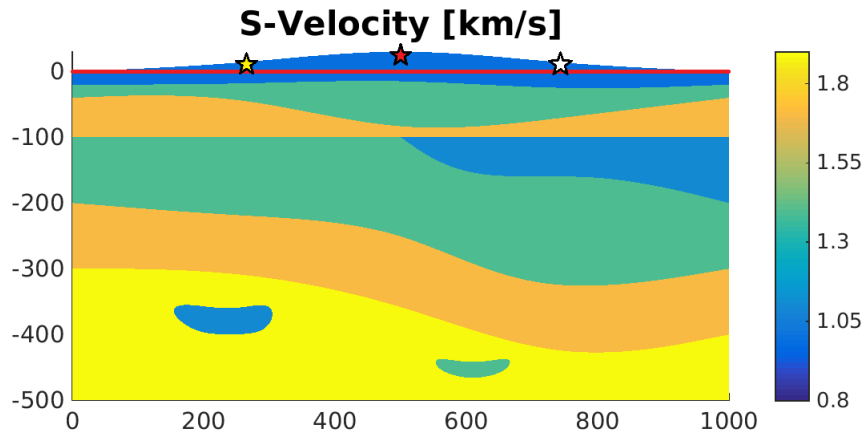
Figure 3.12: Complex near-surface model with material S-wave velocity. (a) model contains 7 layers with curved free-surface, and 9 collapsed karst structures as velocity anomalies. (b) model as same as (a) except the existence of 7 shallow collapsed karst structured as velocity anomalies. The minimum value at the shallow velocity anomalies is only 800 m/s, thus it requires small grid spacing despite of large scale earth model. Red line shows the location of receiver line, and stars indicate 3 different locations of seismic sources. The difference between (a) & (b) will show the seismic effect of shallow small size anomalies in the model.

Table 3.3: Size of shallow karst structures as velocity anomalies in complex near-surface earth model (Figure 3.12). The shortest wavelength in the 2nd layer is about 23.3 m, so the length and height of some scatterers are shorter than the wavelength.

Scatterers (from left to right)	Width (m)	Height (m)
1st	24	9
2nd	20	7
3rd	45	16
4th	16	8
5th	19	12
6th	46	16
7th	19	10

be about 23.3 m ($= \text{Vs}/(2 \times f_0) = 1400/60$). Even though the length and height of some scatterers are shorter than the shortest wavelength, the shallow scatterers cause serious noise and mask other reflection signals.

The noises due to the shallow scatterers show similar multiple scattered surface waves to the previous simple test modeling. Since the material inside the scatterers is filled with low-velocity solid materials, some seismic energy of strong direct waves is trapped in scatterers. Even though the scattered waves from 7 scatterers are mixed in the seismograms, the trapped energy inside the scatterers obviously generate multiple scattered surface waves in regular time intervals at the same locations.

Not only the scattered surface waves, but also the effect of curved surface topography and wave dispersion is shown in the complex model seismograms. The curved free-surface distorts the strongest direct surface wave line in the seismogram, so the line is not perfectly straight. If the surface topography were more complex with irregular shape, the direct wave in seismogram would have been distorted more severely just like the results in previous simple test modeling. The surface wave dispersion is also found in the complex model seismograms. Since the first layer has

low-velocity material properties and shallow layers are heterogeneous, direct surface wave dispersion is found in the seismograms. These dispersion waves also cause scattering at the shallow scatterers, so we can find them in the seismogram of difference despite their weak amplitude.

Although the scattered waves in the complex earth model cannot be identified exactly, seismic analysis of the previous simple test models were useful to infer that complex waves. Seismic effect of those factors: filling material inside the scatterers, irregular surface topography, surface wave dispersion due to shallow heterogeneous layers, are analyzed in both simple and complex synthetic near-surface models. The different modeling grid design and attenuation factor, Q are not applied to the complex model this time, but they are also worth attempting for the accurate near-surface models though the modeling is not easy to implement.
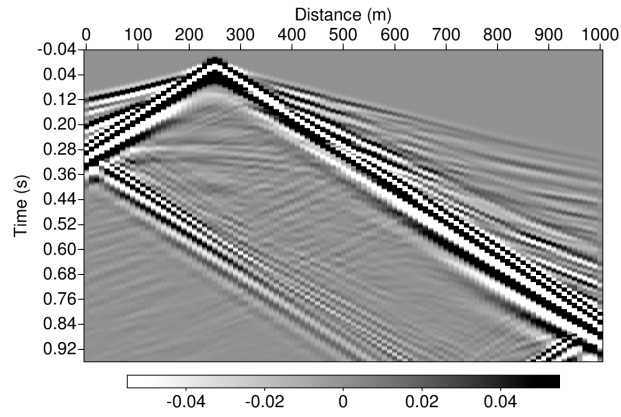
(a)
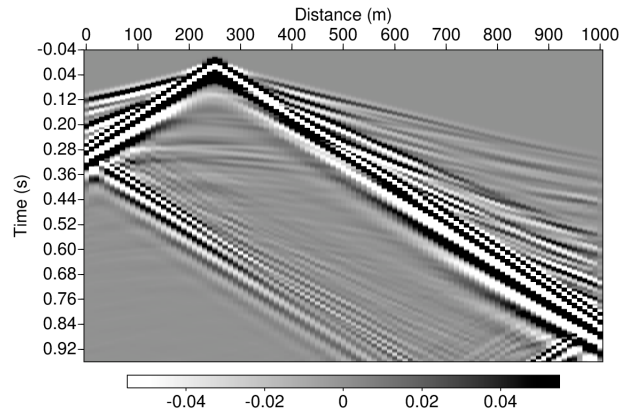
(b)
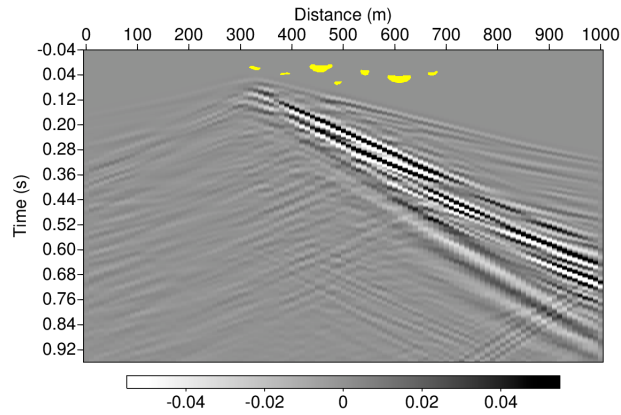
(c)

Figure 3.13: Synthetic seismogram from complex near-surface models. The source location on the x-axis is 250 m as yellow star in Figure 3.12. (a) result from the model with 7 shallow extreme low-velocity anomalies, (b) result from the model without shallow anomalies. (c) differences between the models with/without the shallow scatterers.
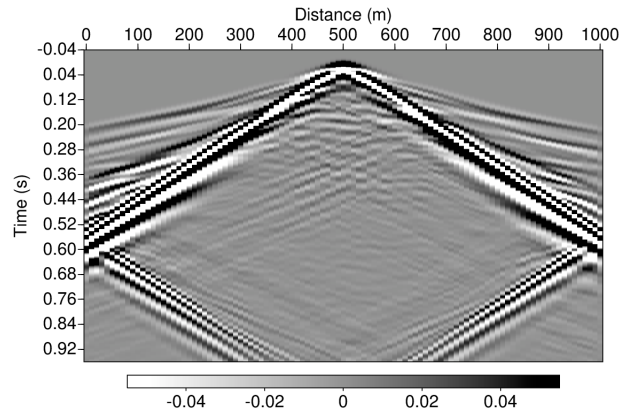
(a)
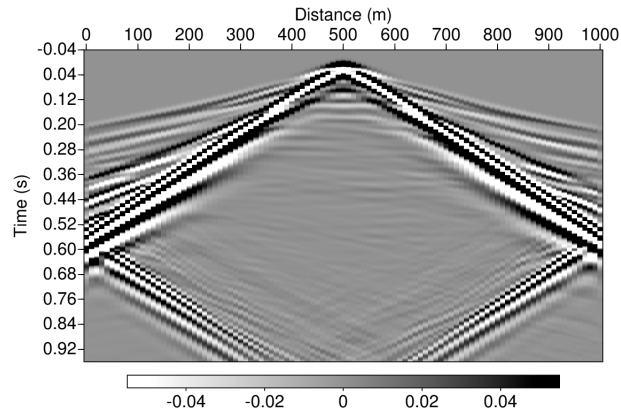
(b)
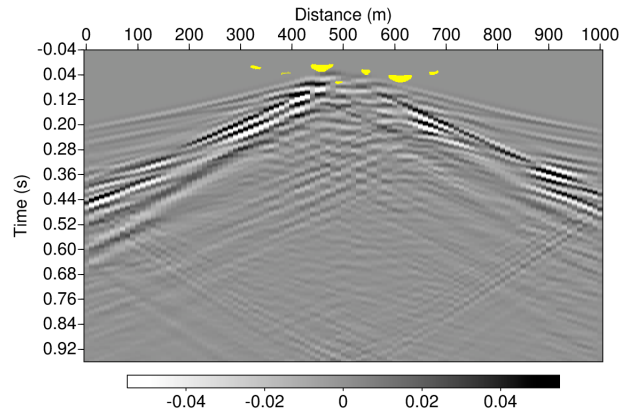
(c)

Figure 3.14: Synthetic seismogram from complex near-surface models. The source location on the x-axis is 500 m as red star in Figure 3.12. (a) result from the model with 7 shallow extreme low-velocity anomalies, (b) result from the model without shallow anomalies.(c) differences between the models with/without the shallow scatterers.
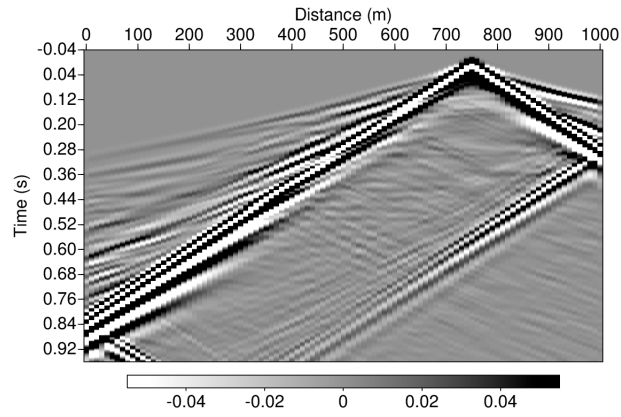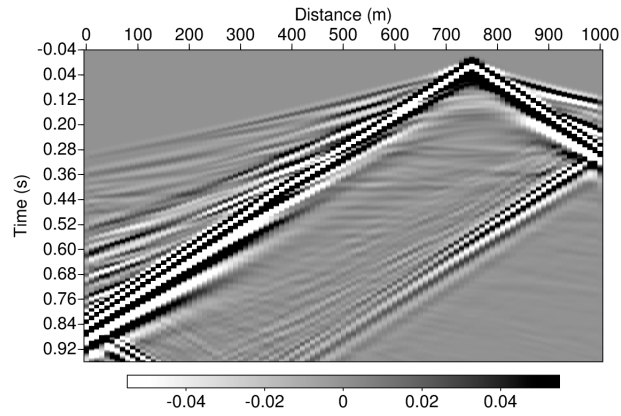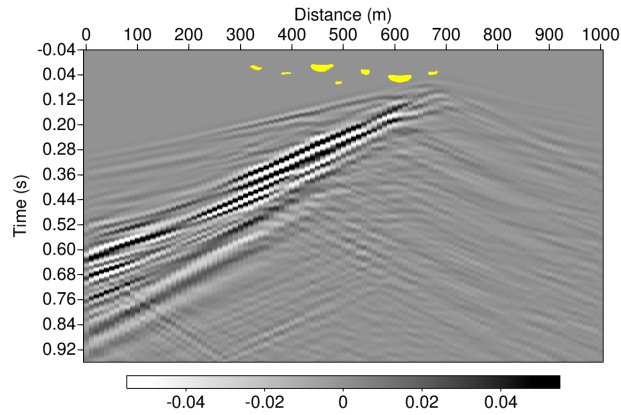
Figure 3.15: Synthetic seismogram from complex near-surface models. The source location on the x-axis is 750 m as white star in Figure 3.12. (a) result from the model with 7 shallow extreme low-velocity anomalies, (b) result from the model without shallow anomalies.(c) differences between the models with/without the shallow scatterers.

4. DISCUSSION

The benefit of the spectral-element method with locally-refined hybrid grids in near-surface modeling have been discussed. Even though the unstructured grids on irregular surface topography show more accurate results, we need to consider the computational costs too. To estimate the efficiency of the spectral-element method, a conventional finite-difference method is compared as a reference solution. An open source code seismic CPML is used with 4th order accuracy, and the same size simple model is implemented by both this code and SPECFEM2D based on the spectral-element method. The simulation running times have linear relations to the total number of cells in entire model. Thus, a small scale model is used to compare two different algorithms. Because of small time steps in the spectral-element method due to high order basis functions, it takes about 5 times longer to run the simple model than the 4th order finite-difference method. However, the potential possibility from locally-refined grids in the spectral-element method should be considered in a large scale earth model, such as the SEAM 2 project "arid model"($10 \ km\times 3.75 \ km$).

Based on the minimum value of S-wave velocity in the earth model is about 400 m/s, I assumed that the Ricker wavelet source has 30 Hz dominant frequency, and the finite-difference method needs at least 10 cells in the shortest wavelength to get accurate enough results. On the other hand, the spectral-element method requires only five cells in the shortest wavelength; the total number of cells in the entire model must be smaller than the cells for the finite-difference method. Furthermore, locally-refined grids can be used in the spectral-element method, so I assumed the fine grid spacing (1 m) only applied upto 200 m depth from the surface. The grid cell size in the finite-difference method should be 0.5 m on entire model, but in the

39

spectral-element method, the grid spacing size has both fine 1 m and coarse 4 m. If we need a large scale earth model as 10 $km\times$ 3.75 km, the finite-difference method needs 20,000 × 7,500 (= 150,000,000) cells, but the spectral-element method requires only 7,062,500 cells. The cell numbers in finite-difference method is about 20 times larger than that of the spectral-element method.

Since the finite-difference method requires 20 times as many cells and is about 5 times faster than the spectral-element method, the spectral-element method would be 4 times faster to handle a large scale near-surface model to implement wave propagation simulation. This rough discussion shows that using the spectral-element method has more benefits in both accuracy and efficiency than the finite-difference method to obtain authentic results for accurate near-surface modeling and analysis of scattered surface wave field.

Table 4.1: Comparison of simulation running time.

	Finite-difference	Spectral-element method
Cells per wavelength	10	5
Cell size	$0.5m$	$1 \sim 4m$
Totam cells	$20,000 \times 7,500$	$7,062,500$
Ratio of cell number	21.2 n	n
Time for same model size	0.2 t	t
Estimated simulation time	4 T	T

5. CONCLUSION

Numerical simulation of elastic wave propagation is implemented based on the spectral-element method and shows the seismic effects from near-surface anomalies. Locally-refined hybrid grids are applied to represent the complex geometry of the subsurface structures and irregular surface topography. This approach shows more accurate results and has the potential to reduce excessive computational costs. The complex hybrid grids are generated by using commercial software CUBIT, and the spectral-element method as an effective high-order finite-element method can utilize these unstructured grids in complex near-surface earth models. Various synthetic near-surface earth models are used, and the resulting seismograms from each case study are interpreted. The collapsed karst structure model shows S-wave distortion at the edge of its boundary, and the shallow small size scatterer acts as a secondary source generating scattered surface waves. Since both structures are filled with low-velocity materials, they generate unwanted seismic waves and corrupt the seismic data quality.

The size of shallow scatterer in the near-surface modeling is very small, but it causes a significant seismic effects. It is filled with low-velocity materials, and a large amount of seismic energy from the direct surface wave is trapped in it. This energy continuously generates multiples and masks the upcoming signals, which we really need to identify. The trapped energy inside the scatterer is sensitively affected by shape of modeling grids and filling material properties. The resulting seismogram of unstructured grid model, which has more benefits in drawing complex geometry of the scatterer, shows differences of wave amplitude from that of the conventional regular Cartesian grid model. The result from the regular Cartesian grid model

causes artificial larger amplitude of scattered waves, and the trapped energy amount is smaller than that of the unstructured grid model. This indicates that forward modeling should handle unstructured conforming grids instead of regular Cartesian grids to obtain more accurate results. The different materials also show different scattered surface wave propagation. The high-velocity solid scatterer and air-filled cavity show weak scattered surface waves because there is no trapped seismic energy inside the scatterer. However, the low-velocity solid scatterer and water-filled cavity contain high amplitude seismic energy and generate complex multiple scattered surface waves. In the past, we considered an air-filled cavity as a water-filled cavity because both are acoustic materials. However, this study shows that the analysis of trapped energy inside the scatterer is more important than identifying the filling materials.

Seismic effects of attenuation, curved topography and low-velocity top layer are also considered to analyze more accurate scattered surface waves. As the number of attenuation factor Q in forward modeling decreasing, the amplitude of multiple scattered waves from the trapped energy in shallow scatterer decreases. The geometry of curved topography can also generate scattered surface waves, which can be misunderstood as the effect of shallow scatterer. The discontinuous direct surface wave in the seismogram can be used to identify the existence of irregular free-surface topography. The low-velocity top layer, which is common in arid regions, causes surface wave dispersion and severely corrupts the signals. However, the seismic effects of karst structure and shallow scatterer as subsurface velocity anomalies are obvious in each seismogram, and the characteristic of wave propagation due to velocity anomalies are similar to that from the simple synthetic modelings.

Since scattered surface waves are sensitively affected by various geological features and modeling factors, advanced seismic forward modeling approaches should

be used for the near-surface modeling. In this study, the spectral-element method with locally-refined hybrid grids shows the capability and potential to overcome the challenging heterogeneity problems in the near-surface modeling. I expect that this study can lead to better distinguishing seismic noise caused by shallow anomalies from valuable signals. Accurate near-surface modelings will be used for seismic acquisition and data processing in arid karst regions, and improve surface wave validations for imaging upcoming P-waves associated with hydrocarbon reservoirs.

REFERENCES

Aki, K., and P. G. Richards, 2002, Quantitative seismology: Sausalito, CA, United States: University Science Books.

Al-Husseini, M. I., J. B. Glover, and B. J. Barley, 1981, Dispersion patterns of the ground roll in eastern Saudi Arabia: Geophysics, **46**, 121–137.

Almalki, H., and K. Munir, 2013, Efficiency of seismic attributes in detecting near-surface cavities: Arabian Journal of Geosciences, **6**, 3119–3126.

Almuhaidib, A. M., and M. N. Toksoz, 2014, Numerical modeling of elastic- wave scattering by near- surface heterogeneities: Geophysics, **79**, T199–T217.

Appelo, D., and N. Petersson, 2009, A stable finite difference method for the elastic wave equation on complex geometries with free surfaces: Communications in Computational Physics, **5**, 84–107.

Bohlen, T., and E. H. Saenger, 2006, Accuracy of heterogeneous staggered-grid finite-difference modeling of Rayleigh waves: Geophysics, **71**, T109–T115.

Bridle, R., R. Ley, and A. Al-Mustafa, 2007, Near- surface models in Saudi Arabia: Geophysical Prospecting, **55**, 779–792.

Casarotti, E., M. Stupazzini, S. J. Lee, D. Komatitsch, A. Piersanti, and J. Tromp, 2008, Cubit and seismic wave propagation based upon the spectral-element method: An advanced unstructured mesher for complex 3d geological media: Proceedings of the 16th International Meshing Roundtable, 579–597. (Bgv54 Times Cited:7 Cited References Count:18).

Chung, E., Y. Efendiev, and R. Gibson, 2011, Multiscale finite element modeling of acoustic wave propagation: SEG Technical Program Expanded Abstracts, **30**, 2898–2903.

De Basabe, J. D., and M. K. Sen, 2007, Grid dispersion and stability criteria of some common finite-element methods for acoustic and elastic wave equations: Geophysics, **72**, T81–T95. (237PF Times Cited:42 Cited References Count:40).

Galvez, P., J. P. Ampuero, L. A. Dalguer, S. N. Somala, and T. Nissen-Meyer, 2014, Dynamic earthquake rupture modelled with an unstructured 3-d spectral element method applied to the 2011 m9 Tohoku earthquake: Geophysical Journal International, **198**, 1222–1240. (Am2yn Times Cited:0 Cited References Count:73).

Gelis, C., D. Leparoux, J. Virieux, A. Bitri, S. Operto, and G. Grandjean, 2005, Numerical modeling of surface waves over shallow cavities: Journal of Environmental and Engineering Geophysics, **10**, 111–121.

Gibson, Richard L., J., K. Gao, E. Chung, and Y. Efendiev, 2014, Multiscale modeling of acoustic wave propagation in 2d media: Geophysics, **79**, T61–T75.

Graves, R. W., 1996, Simulating seismic wave propagation in 3d elastic media using staggered-grid finite differences: Bulletin of the Seismological Society of America, **86**, 1091–1106.

Keho, T. H., and P. G. Kelamis, 2012, Focus on land seismic technology: The near-surface challenge: Leading Edge (Tulsa, OK), **31**, 62–68.

Kelly, K. R., R. W. Ward, S. Treitel, and R. M. Alford, 1976, Synthetic seismograms: A finite-difference approach: Geophysics, **41**, 2–27.

Komatitsch, D., C. Barnes, and J. Tromp, 2000, Wave propagation near a fluid-solid interface: A spectral-element approach: Geophysics, **65**, 623–631. (304NR Times Cited:57 Cited References Count:29).

Komatitsch, D., and J. Tromp, 1999, Introduction to the spectral element method for three-dimensional seismic wave propagation: Geophysical Journal International, **139**, 806–822. (265BP Times Cited:296 Cited References Count:61).

Komatitsch, D., and J. Tromp, 2002a, Spectral- element simulations of global seismic

wave propagation - i. validation: Geophysical Journal International, **149**, 390–412.

Komatitsch, D., and J. Tromp, 2002b, Spectral- element simulations of global seismic wave propagation - ii. three-dimensional models, oceans, rotation and self-gravitation: Geophysical Journal International, **150**, 303–318.

Komatitsch, D., and J. Tromp, 2003, A perfectly matched layer absorbing boundary condition for the second-order seismic wave equation: Geophysical Journal International, **154**, 146–153. (690AE Times Cited:105 Cited References Count:38).

Komatitsch, D., S. Tsuboi, and J. Tromp, 2005, The spectral-element method in seismology: Seismic Earth: Array Analysis of Broadband Seismograms, **157**, 205–227. (Boh96 Times Cited:33 Cited References Count:79 Geophysical Monograph Series).

Komatitsch, D., and J. P. Vilotte, 1998, The spectral element method: An efficient tool to simulate the seismic response of 2d and 3d geological structures: Bulletin of the Seismological Society of America, **88**, 368–392. (Zj391 Times Cited:382 Cited References Count:95).

Lee, S. J., H. W. Chen, Q. Y. Liu, D. Komatitsch, B. S. Huang, and J. Tromp, 2008, Three-dimensional simulations of seismic-wave propagation in the Taipei basin with realistic topography based upon the spectral-element method: Bulletin of the Seismological Society of America, **98**, 253–264. (267FF Times Cited:31 Cited References Count:24).

Liu, T., M. K. Sen, T. Y. Hu, J. D. De Basabe, and L. Li, 2012, Dispersion analysis of the spectral element method using a triangular mesh: Wave Motion, **49**, 474–483. (937DG Times Cited:6 Cited References Count:40).

Luo, Y., H. Zhu, T. Nissen-Meyer, C. Morency, and J. Tromp, 2009, Seismic modeling and imaging based upon spectral-element and adjoint methods: Leading Edge (Tulsa, OK), **28**, 568–574.

Ma, S., R. J. Archuleta, and P. Liu, 2004, Hybrid modeling of elastic p- sv wave motion: A combined finite-element and staggered-grid finite-difference approach: Bulletin of the Seismological Society of America, **94**, 1557–1563.

McNeely, J., T. Keho, T. Tonellot, R. Ley, and J. Chen, 2012, 3d acoustic waveform inversion of land data: A case study from saudi arabia.

Metwaly, M., and F. Alfouzan, 2013, Application of 2-d geoelectrical resistivity tomography for subsurface cavity detection in the eastern part of Saudi Arabia: Geoscience Frontiers, **4**, 469–476.

Muir, F., J. Dellinger, J. Etgen, and D. Nichols, 1992, Modeling elastic fields across irregular boundaries: Geophysics, **57**, 1189–1193.

Oristaglio, M., 2012, Seam update: Seam phase iisurface waves in land seismic exploration: The Leading Edge, **31**, 1130–1132.

Park, C., R. D. Miller, and J. Xia, 1999, Multichannel analysis of surface waves: Geophysics, **64**, 800–808.

Patera, A. T., 1984, A spectral element method for fluid-dynamics - laminar-flow in a channel expansion: Journal of Computational Physics, **54**, 468–488. (Sx220 Times Cited:833 Cited References Count:19).

Peters, W. D., J. J. Pint, and N. Kremla, 1990, Karst landforms in the kingdom of Saudi Arabia: NSS Bulletin, **52**, 21–32.

Reshetova, G. V., V. V. Lisitsa, V. A. Tcheverda, and V. A. Pozdnyakov, 2011, Impact of cavernous/ fractured reservoirs to scattered seismic waves in 3d heterogeneous media: Accurate numerical simulation and field study: SEG Technical Program Expanded Abstracts, **30**, 2875–2880.

Robertsson, J., 1996, A numerical free- surface condition for elastic/viscoelastic finite-difference modeling in the presence of topography: Geophysics, **61**, 1921–1934.

Seriani, G., and E. Priolo, 1991, High-order spectral element method (spem) for acoustic wave propagation.

Shearer, P. M., 1999, Introduction to seismology: Cambridge, United Kingdom: Cambridge University Press.

Tessmer, E., D. Kosloff, and A. Behle, 1992, Elastic wave- propagation simulation in the presence of surface-topography: Geophysical Journal International, **108**, 621–632.

Xia, J., R. D. Miller, and C. Park, 1999, Estimation of near- surface shear- wave velocity by inversion of Rayleigh waves: Geophysics, **64**, 691–700.

Yilmaz, O., 2013, An image- based effective- medium modeling of near-surface anomalies: Leading Edge, **32**, 394–401.

Zeng, C., J. Xia, R. D. Miller, and G. P. Tsoflias, 2012, An improved vacuum formulation for 2d finite-difference modeling of rayleigh waves including surface topography and internal discontinuities: Geophysics, **77**, T1–T9. ((1,2) (2,3) (2) Geophysics (Geophysics, January 2012, 77(1):T1-T9) Publication Type: Academic Journal; Rights: Copyright 2012 Elsevier B.V., All rights reserved.).

APPENDIX A

SPECTRAL-ELEMENT METHOD

A.1   Theoretical features in the spectral-element method

The goal of seismic wave modeling is to solve the equation of motions in terms of displacement, velocity or acceleration in media. The reference book (Aki and Richards, 2002) shows a general expression derived from elastic theory, and it relates the displacement inside the medium with the stress and external forces acting on the volume. The general equation of wave propagation in simple 1-dimensional medium can be written as the following equation.

$$\rho(x)\frac{\partial^2 u(x,t)}{\partial t^2} - \frac{\partial}{\partial x}\left(\mu(x)\frac{\partial u(x,t)}{\partial x}\right) = f_s(x,t) \tag{A.1}$$

The x is the spatial coordinate and t is the time. $\rho(x)$ is the density, $u(x,t)$ is the displacement field, f_s is an external source and $\mu(x)$ is an elastic coefficient. The line domain model in the spectral-element method is divided into several elements, but they do not have the same length because of GLL points A.3. The elements are non-overlapping but only connected at one grid node. As in the finite-element method, the wave equation in its differential form is not considered. "Weak formulation" is considered in the spectral-element method, and it uses the integrated form of the functions. In the weak formulation, we can see how the model is discretized and how to link the mesh data to the entire model. On each discrete element, we use a rule for the interpolation of functions and corresponding interpolating polynomials. After that, special integration quadrature will be introduced, and this will show us two matrices: elemental mass matrix and elemental stiffness matrix. Then we apply

49

the "assembly" to assign the functions into the correct grid points in the global mesh. We will obtain a linear system of equation to solve the wave propagation.

Let's begin with a 1-dimensional wave equation in an inhomogeneous elastic medium.

$$\rho \frac{\partial^2 u}{\partial t^2} - \frac{\partial}{\partial x}\left(\mu \frac{\partial u}{\partial x}\right) = f \tag{A.2}$$

The first step is to multiply the above equation by a time independent test function $v(x)$ on both sides. This can be any arbitrary function. After that, we integrate the equation, but these steps do not change the solution of the previous equation.

$$v\rho \frac{\partial^2 u}{\partial t^2} - v\frac{\partial}{\partial x}\left(\mu \frac{\partial u}{\partial x}\right) = vf \tag{A.3}$$

$$\int v\rho \ddot{u} dx - \int v \bigtriangledown (\mu \bigtriangledown u)\, dx = \int vf dx \tag{A.4}$$

$$\int v\rho \ddot{u} d\Omega - \int v\mu \bigtriangledown u d\Gamma + \int \bigtriangledown v\mu \bigtriangledown u d\Omega = \int vf d\Omega \tag{A.5}$$

The general integration by parts can be derived by the "chain rule" and the "Gaussian divergence theorem." The boundary in a 1-dimensional domain only consists of two points, and we use the free-surface boundary condition, which means a zero-stress condition on these boundary points.

$$\int \mu \bigtriangledown u d\Gamma = \mu \left.\frac{\partial u}{\partial x}\right|_{\Gamma} = \sigma_{\Gamma} = 0 \tag{A.6}$$

The final form of the weak formulation will be the equation below. This is the "weak

form" of the 1-dimensional wave equation.

$$\int v\ddot{u}dx + \int \nabla v\mu \nabla u dx = \int v f dx \qquad (A.7)$$

The next step is to solve the linear system of equations, and we will use the Gauss-Lobatto-Legendre (GLL) quadrature of order N. The model domain has to be divided into n_e elements, and certain rules to create a solid match between mesh and corresponding elements will be used. This process is usually tricky and time consuming; however, this constitutes the advantage of the spectral-element method over conventional finite-difference methods.
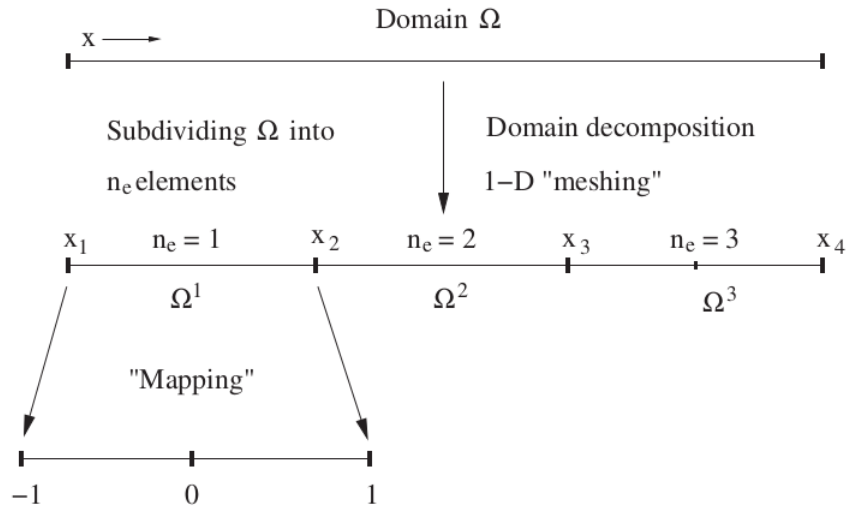

Figure A.1: 1-dimensional domain decomposition and mapping. The line domain is divided into three elements in this figure.

Figure A.1 shows the idea of dividing the entire domain Ω into elements. Each element is transformed, and mapped onto the standard interval $[-1, 1]$ of the GLL integration quadrature. This "mapping function" transforms the "global" coordinates

into "local" coordinates. Generally, the mapping is done by using shape functions, which interpolates the solution between the discrete values obtained at the mesh nodes.

Figures A.2 shows the simple Lagrange polynomials of degree $N = 1$ and 2 as shape functions in the 1-dimensional spectral-element method. The shape functions can be written as below.

$$l_0(\xi) = \frac{\xi - (+1)}{-1 - (+1)} = -\frac{\xi - 1}{2}, l_1(\xi) = \frac{\xi - (-1)}{1 - (-1)} = \frac{\xi + 1}{2} \tag{A.8}$$

Even though the above shape functions are simple, typically, degree $N = 4 \sim 8$ is chosen for the polynomials in the spectral-element method to calculate more accurate results. Using the same points for interpolation and integration is the key feature of the spectral-element method to efficiently use these high-order Lagrange polynomials. The Lagrange polynomials can be generally defined as below.

$$l_i^N = \prod_{j=0, j \neq i} \frac{\xi - \xi_j}{\xi_i - \xi_j} \tag{A.9}$$

These Lagrange polynomials have an important characteristic. Each polynomial has exactly the value 1 at the coordinate x_i and exactly 0 at all other nodes in the element. Between the points, the polynomial can have any value, but it should be continuous.

A.2 Simple numerical test to compare the traditional high-order finite-element method and the spectral-element method

Many published papers have explained the theoretical features of the spectral-element method, but none of them show simple examples of comparison between the traditional high-order finite-element method and the spectral-element method.
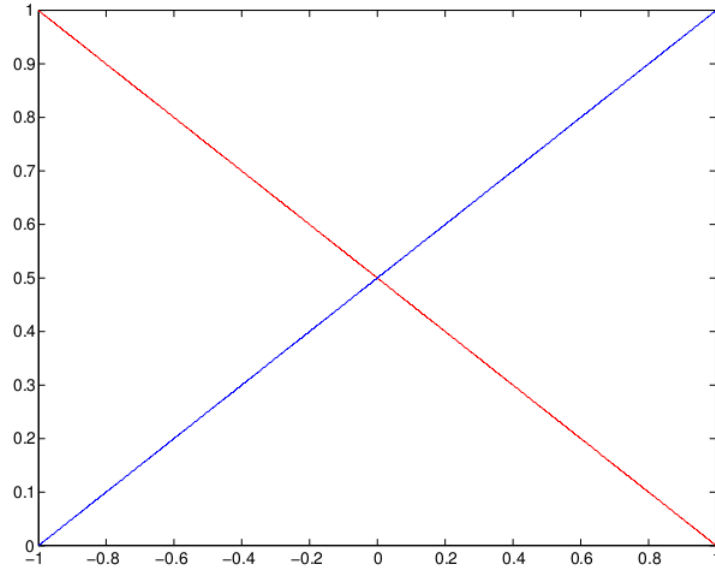
(a)

(b)

Figure A.2: Shape functions of each polynomial degree N. (a) $N = 1$, (b) $N = 2$
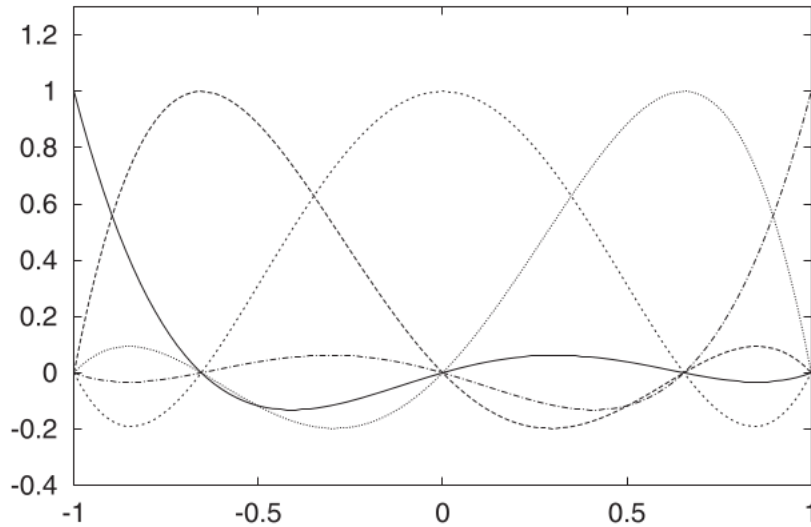
Figure A.3: Lagrange interpolation of degree $N = 4$ on the reference segment $[-1,$ 1]. The $5(= N + 1)$ Gauss-Lobatto-Legendre points can be distinguished along the horizontal axis. All Lagrange polynomials are, by definition, equal to 1 or 0 at each of these points. Note that the first and last points are exactly -1 and 1 (Komatitsch et al., 2005).

The exact diagonal mass matrix is the key point of the spectral-element method, so a simple numerical test is implemented to show the local mass matrices in both algorithms. Figure A.4 shows the plot from the numerical test to calculate the function $arctangent((x - 0.8) \times 50)$. This shows the effect of "h-p refinement" in the finite-element method, which increases the number of degrees of freedom (DOF) to get more accurate results. Simple 1-dimensional domain x from 0 to 1 is divided into 5 sections of uniform grid, and the analytic solution is shown in blue curve line for reference.

Figure A.4-a as "h-refinement" shows the accuracy change with the increasing number of elements. The L2 norm percentages are calculated to show the number of errors in the numerical test based on the analytical solution. As the number of
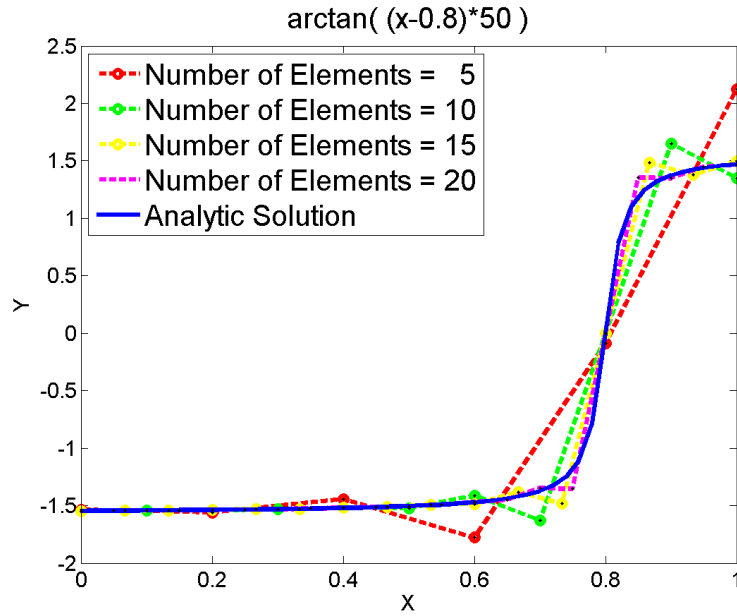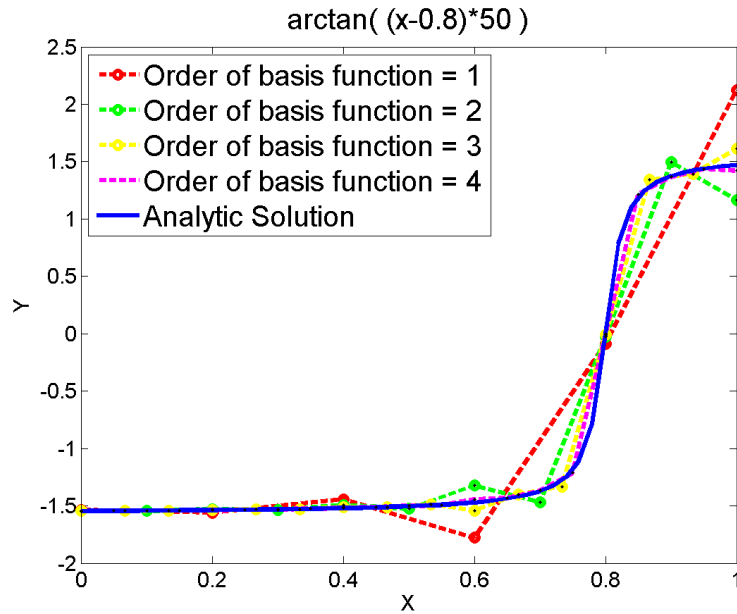
Figure A.4: Plots of simple numerical tests to show "h-p refinement". (a) "h-refinement", which refers to making a mesh finer, and (b) "p-refinement", which refers to increase the order of basis function polynomials while the number of mesh cells remains the same.
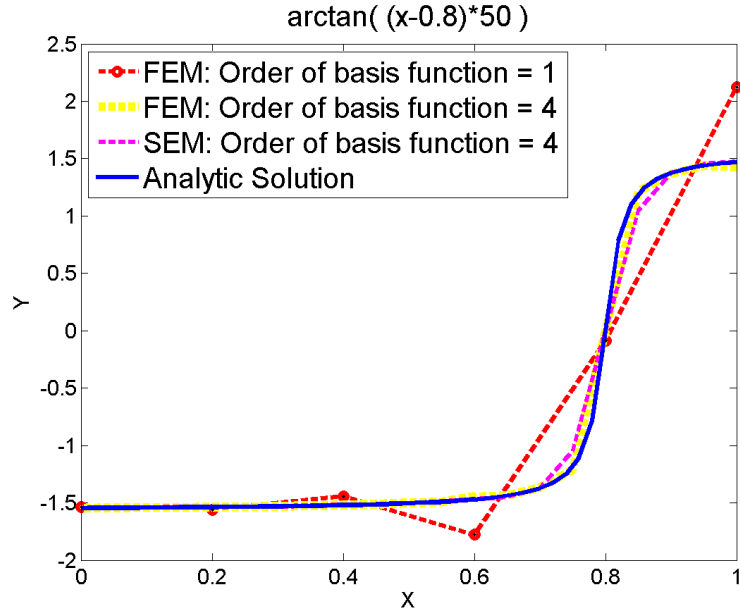
Figure A.5: Plot of a simple numerical test to compare the finite-element and the spectral-element method. Both algorithms, based on the same high-order (4th) basis function, show similar results, and they are shown in Table A.1.

elements increase from 5, 10, 15 to 20, the L2 norm decreases: 8.91, 2.37, 0.81 to 0.32. The increasing order of basis function also demonstrates similar results. Figure A.4-b as "p-refinement" shows the accuracy change from increasing the order of basis function in the traditional finite-element method. As the order increase from 1st to 4th, then the L2 norm decreases: 8.91, 1.46, 0.30 to 0.13. The increase of DOF shows the improved accuracy of the numerical calculation, but the calculation running time should be considered as a computational cost.

This result of the high-order basis function finite-element method is compared with the result based on the spectral-element method (Figure A.5). Both algorithms use the same number of elements and the same basis function order as 4th. The difference between the two algorithms is only the integration rules, which is the traditional Gaussian-Legendre rule in the finite-element method and the Gaussian-

Table A.1: Comparison the finite-element and the spectral-element methods in accuracy & efficiency in Figure A.3. 4th order based calculation by the finite-element and the spectral-element methods show different results. The accuracy of the finite-element method is a little bit higher than the spectral-element method, but the simulation running time of the spectral-element method is faster than the finite-element method.

Algorithm	Order of basis function	L2 norm	Time (ms)
FEM	1st	8.91	10.6
FEM	4th	0.13	37.9
SEM	4th	0.49	32.1

Table A.2: One of 5×5 size local mass matrices in simple numerical test calculation. (a) matrix from the finite-element method, and (b) matrix from the spectral-element method. The matrix in the spectral-element method (b) is exactly diagonal matrix, which makes the simulation faster than the traditional finite-element method.

		(a)					(b)		
Finite-Element Method					Spectral-Element Method				
1.0	1.0	-0.6	0.2	-0.1	$+1.0$	0.0	0.0	0.0	0.0
1.0	6.3	-1.4	0.9	0.2	0.0	$+5.4$	0.0	0.0	0.0
-0.6	-1.4	6.6	-1.4	-0.6	0.0	0.0	$+7.1$	0.0	0.0
0.2	0.9	-1.4	6.3	1.0	0.0	0.0	0.0	$+5.4$	0.0
-0.1	0.2	-0.6	1.0	1.0	0.0	0.0	0.0	0.0	$+1.0$

Lobatto-Legendre rule in the spectral-element method. The results of this comparison are presented in Table A.1. The L2 norm from the high-order finite-element method is 0.13 and the L2 norm from the spectral-element method is 0.49. Even though the L2 norm value from the spectral-element method is a little higher than that of the finite-element method, it shows less running time. The running time difference shows a small value in this test, but in 3 dimensional simulations, this must be an important factor to reduce the simulation running time from large-scale modeling. This is caused by the mass matrix, and one of the local mass matrices in both algorithms is shown in Table A.2. We can see that the mass matrix in the spectral-element method shows exactly diagonal matrix (Table A.2-b).

A.3 Gauss-Lobatto-Legendre collocation points and integration weights

Table A.3: Polynomial degree in spectral-element method, collocation points and integration weights of Gauss-Lobatto Legendre quadrature.

Polynomial Degree N	Collocation Points x_i	Integration weights w_i
2	0	1.3333
	$\pm$ 1.0000	0.3333
3	$\pm$ 0.4472	0.8333
	$\pm$ 1.0000	0.1667
4	0	0.7111
	$\pm$ 0.6547	0.5444
	$\pm$ 1.0000	0.1000
5	$\pm$ 0.2852	0.5549
	$\pm$ 0.7651	0.3785
	$\pm$ 1.0000	0.0667
6	0	0.4876
	$\pm$ 0.4688	0.4317
	$\pm$ 0.8302	0.2768
	$\pm$ 1.0000	0.0476
7	$\pm$ 0.2093	0.4125
	$\pm$ 0.5917	0.3411
	$\pm$ 0.8717	0.2107
	$\pm$ 1.0000	0.0357

APPENDIX B

SUPPLEMENTARY MEDIA FILES

Supplementary movie files for this thesis show the simulations of elastic wave propagation in various near-surface models for this research. The movies from the complex near-surface model with different source locations are listed as below.

movie_nearSurface_TopoModel_srcX250_SEM.avi: Shows the wave propagation on the model of Figure 3.12-a with a source on the free-surface located at 250 m in x-axis.

movie_nearSurface_TopoModel_srcX500_SEM.avi: Shows the wave propagation on the model of Figure 3.12-a with a source on the free-surface located at 500 m in x-axis.

movie_nearSurface_TopoModel_srcX750_SEM.avi: Shows the wave propagation on the model of Figure 3.12-a with a source on the free-surface located at 750 m in x-axis.

Additional simulation movie files were uploaded to analyze the seismic waves through a big size water-filled cavity and an air-filled cavity. The diameter is 100 m, and the center depth of the circular cavity is 65 m. Unstructured conforming grids are used to make smooth boundary of the circular cavity.

air_BigCavity_DispX_SEM2.avi: Shows the horizontal component displacement of the wave propagation through a big circular shallow air-filled cavity.

air_BigCavity_DispZ_SEM2.avi: Shows the vertical component displacement of the wave propagation through a big circular shallow air-filled cavity.

water_BigCavity_DispX_SEM2.avi: Shows the horizontal component displacement of the wave propagation through a big circular shallow water-filled cavity.

water_BigCavity_DispZ_SEM2.avi: Shows the vertical component displacement of the wave propagation through a big circular shallow water-filled cavity.